Stellar evolution through cosmic ages: Extending the BoOST stellar model grids

Master Thesis

Author: Hanno Stinshoff (Student ID: 5578957)
Supervisor: Prof. Dr. Stefanie Walch-Gassner (University of Cologne, Germany)
Co-Supervisor: Dr. Dorottya Szécsi (Nicolaus Copernicus University of Toruń, Poland)

Department of Physics, 1st Institute: Astrophysics
Faculty of Mathematics and Natural Sciences
University of Cologne

25.02.2022

Eidesstattliche Versicherung

Hiermit versichere ich an Eides statt, dass ich die vorliegende Arbeit selbstständig und ohne die Benutzung anderer als der angegebenen Hilfsmittel angefertigt habe. Alle Stellen, die wörtlich oder sinngemäß aus veröffentlichten und nicht veröffentlichten Schriften entnommen wurden, sind als solche kenntlich gemacht. Die Arbeit ist in gleicher oder ähnlicher Form oder auszugsweise im Rahmen einer anderen Prüfung noch nicht vorgelegt worden. Ich versichere, dass die eingereichte elektronische Fassung der eingereichten Druckfassung vollständig entspricht.

Die Strafbarkeit einer falschen eidesstattlichen Versicherung ist mir bekannt, namentlich die Strafandrohung gemäß § 156 StGB bis zu drei Jahren Freiheitsstrafe oder Geldstrafe bei vorsätzlicher Begehung der Tat bzw. gemäß § 161 Abs. 1 StGB bis zu einem Jahr Freiheitsstrafe oder Geldstrafe bei fahrlässiger Begehung.

Hanno Stinshoff

Köln, den 25.02.2022

Acknowledgements

First I would like to thank Prof. Dr. Stefanie Walch-Gassner for having me in her group and providing me with the opportunity to write this thesis. I also appreciate her keeping me focussed on the work through the whole time I worked on it, for providing help in the weekly meetings and for grading my work.
Secondly I want to thank Dr. Dorottya Szécsi for the immense support, many hours of meetings and questions from my part, for believing in me (and expressing that), for reigniting my passion for physics, for grading my thesis and in general for taking care of me.
I also would like to thank the research group of Prof. Dr. Walch-Gassner for the weekly group meetings and helping me get more into the subject in general. Corona may have prevented more in-person contact, but I felt welcome and supported.
I want to thank the University of Cologne. It was a pleasure to study physics. Sometimes it was a hard way, but I am still grateful for the opportunity.
To my parents I want to express my gratitude for supporting me all the way through the studies, be it through highs or lows, supporting me when I needed help and listening to my endless rambles about physics even though I know that it is sometimes hard.
Finally I want to thank all the friends that I made along the way or that kept by my side through it all. I need you and I appreciate you deeply, and I hope you know that.

Tools

The Bonn-Code was used to create the models, gnuplot, gedit and Libre Draw were used for visualisation purposes and LaTeX was used to write down this thesis.

Abstract

The modelling of stellar evolution is a useful tool for astrophysical research.
The models can be used as basis for various investigations like those on their predicted spectra, population synthesis and thus stellar population research. They can be applied to predict stellar feedback while still evolving and also when ending their lives in supernovae and similar explosive fates like in the SILCC project investigating molecular cloud evolution. Also they offer the possibility to see effects in the evolution that would not be observable in nature while in progress due to the long lifetime of a real star.
With new advancements in research, models have to be kept up to date to newer developments, giving opportunity for improvement via new effects discovered or more precise formulas accounting for processes in a star.
The following thesis provides an analysis of multiple newly created evolutionary models of massive stars for the beginning of the main sequence (hydrogen burning).
Around 330 model sequences were created, which differed in initial mass (from 10 to 300 $M_{\odot}$), initial metallicity (from Z_{MW} to 0.02 Z_{SMC}) and initial rotational velocity (0 to 500 km/s) to create a grid in a 3D parameter space. The model computations end at a point of 60% of the hydrogen burning. These new models fill in gaps in the parameter space of the recently published BoOST model grids for low metallicities, high masses and high rotational velocities, giving an overview of the different parameter configurations.
Comparing the models highlights the differences in the evolution, especially noteworthy being the chemically homogeneous evolution, which is predominantly found in metal-poor areas for stars with high rotation and mass, and the Cool Supergiant phase, presenting inflated stars with a comparably cool temperature.
With these models, possibly continued further in the future and with an increased parameter resolution in critical areas, there are many possibilities for application.

Contents

List of Figures

List of Tables

Abbreviation Index

Abbreviation	Meaning
I Zw 18	I Zwicky 18 (A dwarf galaxy with $Z = 0.02\,Z_{MW}$)
BEC	Binary evolutionary code
BoOST	Bonn Optimized Stellar Tracks (see also: BEC)
CHE	Chemically homogeneous evolution
EEP	Equivalent evolutionary phases
GRB	Gamma ray burst
HRD	Hertzsprung-Russell diagram
IMF	Initial mass function
ISM	Interstellar medium
LMC	Large magellanic cloud
MW	Milky Way
NE	Normal evolution (see also: CHE, TE)
PICO shell	Photo Ionisation COnfined shell
PoWR	Potsdam Wolf-Rayet
RGB	Red Giant Branch
RSGB	Red Supergiant Branch
SILCC project	SImulating the Life-Cycle of molecular Clouds
SMC	Small magellanic cloud
SLSN	Superluminous Supernova (see also: Supernova)
SN	Supernova
TE	Transitional evolution
TWUIN	Transparent Wind Ultraviolet intense stars
Y_C	Core helium mass fraction
Y_S	Surface helium mass fraction
ZAMS	Zero age main sequence

Table 1: Abbreviation index for the following work, in alphabetical order of the abbreviations

1 Motivation

Astronomy is a fascinating topic to humanity for a long time. Even in times of the Old Stone Age some eyes were fixed to the sky, and the interest did not vanish until today (cf. the introduction and chapter 9.1 of Demtröder 2014).
Naturally we know a lot more about what we see today; there are better telescopes to investigate, better computation resources for modelling and better understanding of theory and the underlying mathematics.
Nevertheless research is still done all over the world in various areas of Astronomy, with new and better ways to improve it, and there is a lot to be uncovered and understood. Part of that effort is done by modelling of stellar evolution, which is a difficult, yet enlightening procedure. It too is improved upon all the time and changes over the years. Older models (cf. for example Mengel et al. 1979, Pols et al. 1998) are improved on or replaced entirely.
The aim of the thesis at hand was to provide new models for a wide range of input parameters (cf. 2.2.3). As a basis they can be useful for various things:

1.1 SILCC Simulations

The *SImulating the Life-Cycle of molecular Clouds* (SILCC) project is a collaboration of various physicists with the aim to understand and model the evolution of and influences on the interstellar medium (ISM) and life cycles of molecular clouds (cf. Walch et al. 2015). They simulate galactic region boxes as cutouts of galactic discs, caring for various factors of influence like self-gravity, magnetic fields, heating and radiative cooling, chemistry of molecules like H_2 and CO and supernova feedback. For this they need new and accurate models of stars in different environments and states (like metallicities and rotational velocities) as the basis of their computations for stellar feedback. In Gatto et al. (2016) the authors first implemented such models for massive stars, creating them from sink particles in their simulations, distributed by means of the Salpeter initial mass function (IMF). After that more improvements on that front were applied, one of the latest being covered by the upcoming paper based on Brugaletta (2021), where new metallicities including that of the dwarf galaxy I Zwicky 18 (I Zw 18) were introduced by using models from the *Bonn Optimised Stellar Tracks* (BoOST) project (cf. Szécsi et al. 2022).
The thesis at hand aims to provide even more new models for a wide range of input parameters like mass, rotational velocity and metallicity (cf. 3). The models from BoOST can be added upon by ones with higher velocity, and generally the metallicity resolution can be improved as well.

1.2 Globular Cluster Abundance Anomalies

In *globular clusters* there are known anomalies in the surface abundances of some stars that are giving reason to investigate; some stars show signs of anti-correlations between oxygen and neon or magnesium and aluminium. These stars are not massive (and therefore hot) enough to provide the ability to undergo the CNO-, NeNa- and MgAl-Cycles (cf. Boeltzig et al. 2016) necessary to explain this anti-correlation easily.
For this reason it is at times assumed that those stars are examples of a second generation of stars, fed and polluted by the fusion end product of an older and already extinct generation of stars (cf. Ventura et al. 2011).
To investigate this theory one could use models for the first generation of stars. Works like Szécsi et al. (2018) and Szécsi & Wünsch (2019) provide theories involving cool supergiants as the providers of the abundance anomalies, which would necessitate massive stars. Therefore models for such evolutionary paths are beneficial for the research of such theories.
Additionally the lithium abundance and production can be investigated; as lithium is a product of the pp-chain (cf. 2.1.3) which promptly gets further processed into Helium, finding increased lithium abundances in some stars is something worth investigating. It is assumed to be due to the so-called *Cameron-Fowler mechanism* (cf. Cameron & Fowler 1971). This research can be part of the globular cluster investigation (cf. for example the master theses: Bennett 2018, Ratcliff 2018), but is not limited to it.

1.3 Gamma Ray Bursts

After reaching the end of their lifetime defined by their nuclear fusion stars can reach different states depending on their mass (cf. 2.1.2). Low-mass stars tend to burn up and do not reach temperatures high enough to continue the fusion processes and develop into white dwarves, whereas higher mass stars can continue the fusion until a latter stage and also have different states they develop into, like the neutronstar or even a black hole. Accompanying such a "death" of the star can be phenomena like supernovae or *gamma ray bursts* (GRB, cf. Piran 2005), which are divided into categories based on their energy output and their duration respectively. Especially long duration ($>2\,\mathrm{s}$) GRB and superluminous supernovae (SLSNe) are connected to metal-poor galaxies (cf. Leloudas et al. 2015), which makes stellar evolutionary models for massive, metal-poor stars useful for their investigation.

1.4 Gravitational Wave Research

Since gravitational wave research is now observationally possibly due to the rather new setups like the (advanced) Laser Interferometer Gravitational-Wave Observatory (aLIGO, cf. Aasi et al. 2015), mergers of two massive objects like neutron stars or black holes are detected because of their gravitational waves. This potentially gives rise to many new points of interest, one of which is the research on the distribution of such events. As they arise from mergers of massive objects, a population synthesis would be necessary, so models for a wide range of input parameters would be beneficial. This work aims to provide models ranging in mass and also in other parameters to give a wide range of different models to be applied to a synthetic population.

1.5 Structure

This thesis is structured as follows. First a general overview of the theory is presented in section 2. Here both basic and field-specific information is summarized to provide the necessary knowledge to understand the thesis.
In section 3 the general used initial model parameters are shown, which gives a good perspective on how many were created and what ranges they cover. Also an overview of useful diagrams is presented.
Finally in section 4 the results are presented. Here various aspects are investigated, to be then discussed in section 5. Also an outlook is given to give some more context of the models, which refers back to this section too.

2 Theory

2.1 Stars

Stars are hot spheres of gas that become stable by reaching an equilibrium between the pressure due to gravity and the contrarily pushing gas and radiation pressure (cf. fig. 1).

Gravity derives from the mass of particles that build up the star, which element-

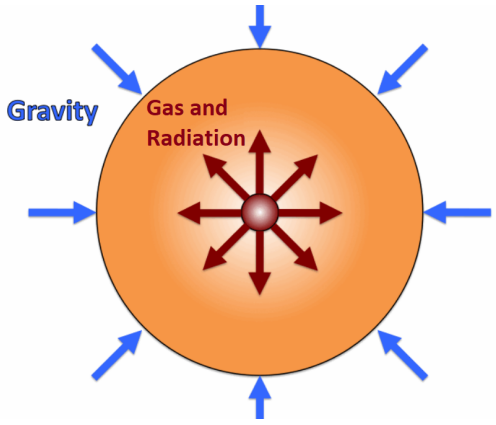

Figure 1: Hydrostatic equilibrium of a star, with the gas- and radiation-pressure (dark red arrows) pushing contrary to the gravitational pressure (blue arrows). Figure altered after taken from Marti et al. (2021)

and isotope-wise vary in abundance. This depends on the star's evolutionary phase, the point in time it was formed, the state of momentum it has and many more physical properties to varying degrees.

The gas exerts an outward pressure due to thermodynamical effects, which results in some amount of resistance to further compression.

On the other hand the radiation pressure arises because the isotopes in the star undergo various different nuclear processes (mostly nuclear fusion), which results in a change of composition abundances and an emission of energy via electromagnetic radiation (cf. Eddington 1988).

Means to quantify the stability of a star and also explanation for behaviour like extended inflation can therefore be the so-called *Eddington limit*; it is the state a star is in when its luminosity is the Eddington luminosity, "which is defined as the condition when the radiative acceleration (g_{rad}) balances the gravitational acceleration (g) at the stellar surface" (cf. Sanyal et al. 2017). Stable stars above the Eddington limit at the surface therefore usually are rarely found in reality (cf. Lamers & Fitzpatrick 1988), it is an upper limit for a stable star's existence, and stars behave differently depending on their closeness to that limit.

This however is a definition based on the surface of the star. It is not easily transferred to the interior, which means that there are stars that inflate (cf. Sanyal et

al. 2015) to supergiants (cf. 2.1.4) because of their high luminosity output.
Before analysing prominent features in stellar evolution one has to note that the evolution can differ significantly depending on the kind of star. Still there are some common features and also some differences that facilitate the differentiation, which will in the following be discussed to be used in the analysis of various models. For that there will be a distinction between a low-mass star (which is a star like the sun in our solar system) and a more massive star (which will be relevant later on).

2.1.1 Metallicity

In the beginning of the first generation of stars only hydrogen and helium were present (cf. Peimbert et al. 2007). Heavier elements were only synthesized in the nuclear fusion processes happening in those stars (cf. 2.1.2, 2.1.3), therefore at the end of their evolution "polluting" their surroundings with that material. The amount of elements heavier than helium is therefore a measure of the time a star started its evolution. This is why *metallicity* Z is an important parameter in astrophysics: It is the mass fraction of elements heavier than helium, in comparison to the fractions for hydrogen X and that for helium Y. It follows that $X + Y + Z = 1$.
Depending on the metallicity the evolution of a star can differ (cf. for example 2.1.5).

2.1.2 Evolutionary Phases

Star formation starts with a cloud of gas (cf. chapter 11.2 and following of Demtröder 2014).
When there are density irregularities due to anisotropies or shockwaves compressing the matter, parts of those clouds start to collapse onto themselves due to gravity. Because of that collapse the region is heating up (which is increasing the gas pressure).
By converting excess energy into radiation and energy used for the ionisation of the gas, the star is preventing unhindered heating. Still the temperature increases and once it approaches a certain point, it is able to initiate the hydrogen burning (cf. 2.1.3) and begin its life as a star and hence its evolution (cf. fig. 2). This point is called the *Zero Age Main Sequence* (ZAMS, cf. next paragraph).
The hydrogen in the star is burned up and fused into helium and heavier elements, the processes responsible differing dependent on the temperature and mass of the star. This process is slower than any following phase of nuclear burning (cf. next paragraph), which gives this phase its name: *Main sequence*.

Once the hydrogen is burned up, the core of a low-mass star contracts (and therefore heats up) until a temperature is reached where it is hot enough to start to fuse helium (helium burning phase). At the same time the envelope expands (and therefore cools down), which leaves the star as a red giant. This gives the phase its name: *Red Giant Branch* (RGB).
The transition between the two phases is rather quick (as can be seen with the lack of isochrone dots in figure 2) and therefore usually not observed as much, as the time spent in this phase is small compared to the main sequence. This is why it is called the *Hertzsprung gap*, because there is a gap of observations in the observational data.
Massive stars however are predicted to expand to the so-called *red supergiant branch* (RSGB) or alternatively to a blue supergiant phase, if they stop expanding while still having a high temperature.
In this phase they use up their helium fuel in the core, sometimes even undergoing so-called blue loops, where, after burning away a significant part of their helium storage while on the RSGB, the stars heat up again to the blue supergiant phase and stay there until the helium in the core is depleted. Then they return to the RSGB (cf. Langer 2012b).
This progression of new fusion processes and subsequent contraction of the core is generally repeated until either the star does not reach the necessary temperatures to initiate new fusion processes and slowly cools to become a dwarf (this trend is more common in low-mass stars), or until not enough energy can be generated (at most at around the iron burning, from where on out fusion does not generate but use up energy) to uphold the radiation pressure necessary to withstand the gravity, therefore resulting in a rapid collapse of the core, which destroys the star with varying end products (neutron stars or black holes after a supernova).
The accumulated time of all phases is also called the *lifetime* of a star.
The time period a star stays in a certain phase of evolution varies. More massive stars tend to spend less time in each phase, which is due to their higher temperatures and the consequently more efficient nuclear processes (cf. 2.1.3).

2.1.3 Nucleosynthesis

The material of stars undergoes various nuclear processes. Since this influences and partly defines different stages of their evolution, some of those processes will be listed here.

Hydrogen Burning: PP-Chains For stars with comparably lower temperature the pp-chain reactions are the dominant processes in the hydrogen-burning phase (cf. Langer 2012a). It starts out with simple ^{1}H Isotopes and reaches ^{4}He

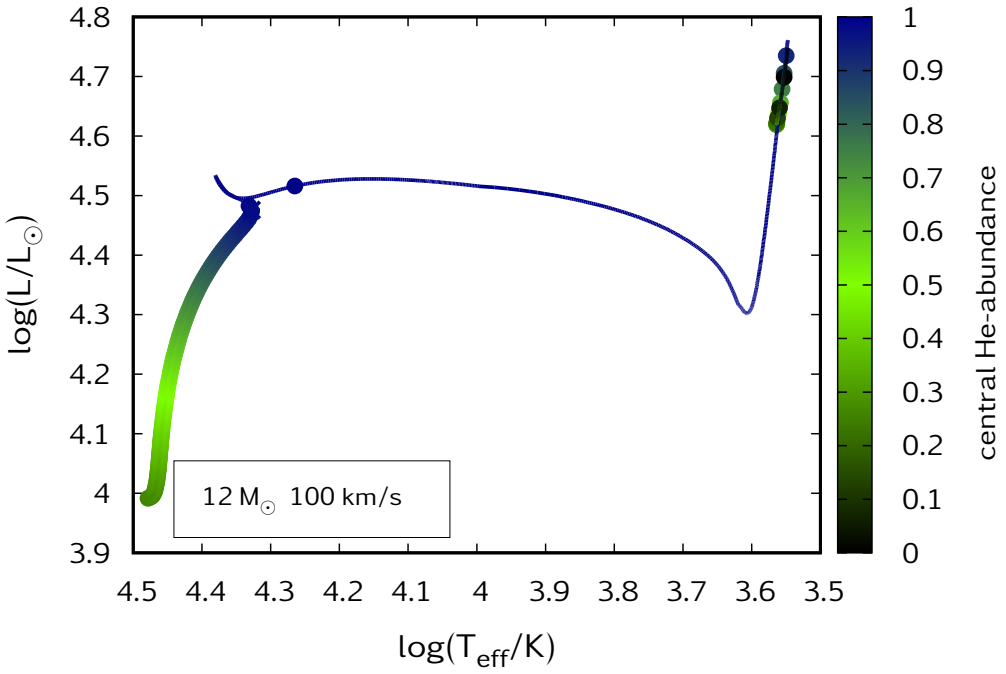

Figure 2: A Hertzsprung-Russell diagram (Plot of Luminosity (in $L_\odot$ with a logarithmic scale) vs. surface temperature (in K, with inversed logarithmic scale, cf. 3.1.1) with isochrone data points (dots) for every 10^5 years over the complete data of the model (line). Colour-coded is the helium abundance in the core. The data is from a simulated $M_{ini} = 12\,M_\odot$ model sequence with LMC metallicity and rotational velocity $v_{rot,ini} = 100\,km/s$ from Szécsi et al. (2022) computed with the Binary Evolutionary Code (BEC). The figure shows the evolution of the model from the beginning of the main sequence (bottom left corner) through the hydrogen burning phase (left vertical arm), then over the Hertzsprung gap (horizontal arm) to the lower surface temperatures, where the helium burning process starts (right vertical arm) and eventually ends (top right corner). Over this evolution one can see the central helium abundance first rising in the main sequence and then decreasing again in the helium burning phase. The isochrone dots emphasize the quick transition over the Hertzsprung gap and the relative durations of main sequence and helium burning phase.

via multiple fusion and beta-decay processes (cf. fig. 3):

$$^1\mathrm{H} + {}^1\mathrm{H} \rightarrow {}^2\mathrm{H} + e^+ + \nu_e \qquad +0.42\,\mathrm{MeV} \qquad (1)$$

$$^2\mathrm{H} + {}^1\mathrm{H} \rightarrow {}^3\mathrm{He} + \gamma \qquad +5.493\,\mathrm{MeV} \qquad (2)$$

$$^3\mathrm{He} + {}^3\mathrm{He} \rightarrow {}^4\mathrm{He} + 2\,{}^1\mathrm{H} \qquad +12.859\,\mathrm{MeV} \qquad (3)$$

This so-called *pp1-chain* is the dominant hydrogen burning process in stars with core temperatures below 20 MK (cf. fig. 5 and Adelberger et al. 2011).

One alternative is the so-called *pp2-chain*, which replaces the last line of equation

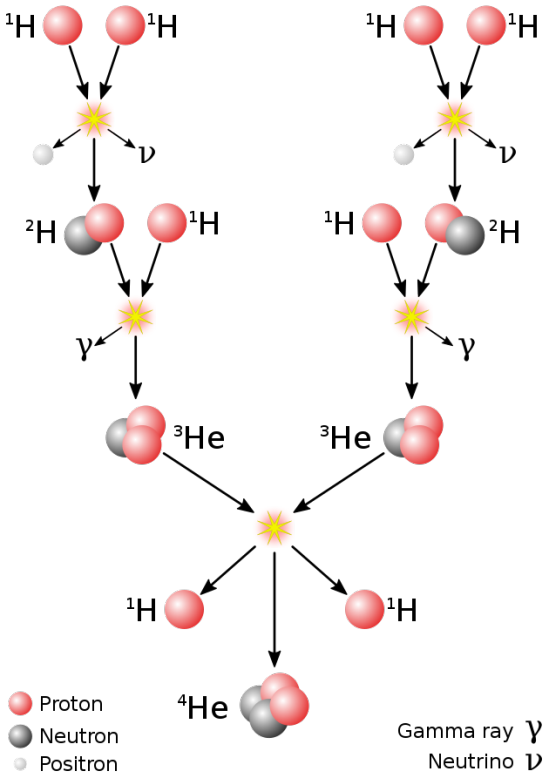

Figure 3: The so-called pp1-chain (cf. eq. 1 and following) is one of the main processes in the hydrogen burning of a star. Here one can see the complete process, starting with single protons (red balls) first (top) undergoing β^+-decay to convert one of the protons into a neutron (grey ball) and emitting a positron (e^+) and a neutrino (ν). Afterwards (middle) another proton gets captured, resulting in ^{3}He and another γ. Finally two of those ^{3}He nuclei transition into a ^{4}He nucleus with two emitted protons (bottom). This last step can also be replaced by the combination of ^{3}He and ^{4}He instead of two ^{3}He nuclei (cf. eq. 4 and following) to get the pp2-chain, which is a relevant source of lithium in a star. Picture taken from Wikimedia Commons.

1 and following with

$$^3\mathrm{He} + {}^4\mathrm{He} \rightarrow {}^7\mathrm{Be} + \gamma \qquad +1.59\,\mathrm{MeV} \qquad (4)$$

$$^7\mathrm{Be} + e^- \rightarrow {}^7\mathrm{Li} + \nu_e \qquad +0.861 \text{ or } 0.383\,\mathrm{MeV} \qquad (5)$$

$$^7\mathrm{Li} + {}^1\mathrm{H} \rightarrow 2\,{}^4\mathrm{He} \qquad +17.35\,\mathrm{MeV} \qquad (6)$$

The pp2-chain is one of the alternatives to the pp1-chain (there are others like for example the pp3-chain, which is irrelevant to this work) and is an important source of lithium in a star. It needs already present helium as a catalyst and also relies on the temperature to induce the fusion to heavier elements like beryllium. As can be seen in equation 4 and following ^{7}Li gets produced and then as a follow up converted again into ^{4}He. If however the temperature of the surroundings of the lithium quickly drops (for example by enhanced mixing in the star, transporting the lithium outside from the hot to the cooler regions of the star), it facilitates the persistence of the lithium in the star and an accumulation. This is called the Cameron-Fowler mechanism (cf. Cameron & Fowler 1971) and it explains increased lithium abundances in low-mass stars. This however would mean that the process of mixing and freeze-out of the lithium would have to happen on a similar timescale to the nuclear one.

Hydrogen Burning: CNO Cycle If heavier elements are already present as catalysts, there are also other possibilities for the star to fuse its hydrogen. One important process is the *CNO cycle* (cf. fig. 4), which uses present carbon, nitrogen and oxygen to fuse the hydrogen to helium:

$$^{12}\mathrm{C} + {}^1\mathrm{H} \rightarrow {}^{13}\mathrm{N} + \gamma \qquad +1.95\,\mathrm{MeV} \qquad (7)$$

$$^{13}\mathrm{N} \rightarrow {}^{13}\mathrm{C} + e^+ + \nu_e \qquad +1.20\,\mathrm{MeV} \qquad (8)$$

$$^{13}\mathrm{C} + {}^1\mathrm{H} \rightarrow {}^{14}\mathrm{N} + \gamma \qquad +7.54\,\mathrm{MeV} \qquad (9)$$

$$^{14}\mathrm{N} + {}^1\mathrm{H} \rightarrow {}^{15}\mathrm{O} + \gamma \qquad +7.35\,\mathrm{MeV} \qquad (10)$$

$$^{15}\mathrm{O} \rightarrow {}^{15}\mathrm{N} + e^+ + \nu_e \qquad +1.73\,\mathrm{MeV} \qquad (11)$$

$$^{15}\mathrm{N} + {}^1\mathrm{H} \rightarrow {}^{12}\mathrm{C} + {}^4\mathrm{He} \qquad +4.96\,\mathrm{MeV} \qquad (12)$$

This process dominates over the pp-chains at temperatures over 20 MK (cf. fig. 5 and Adelberger et al. 2011).

NeNa- and MgAl-Cycle Similar to the CNO cycle there are other cycles that produce helium. There are two especially interesting to the present work, which are depicted in figure 6, namely the *NeNa-* and the *MgAl-Cycle* (cf. Boeltzig et al. 2016). These cycles are for example replenishing the ^{26}Al abundances in the

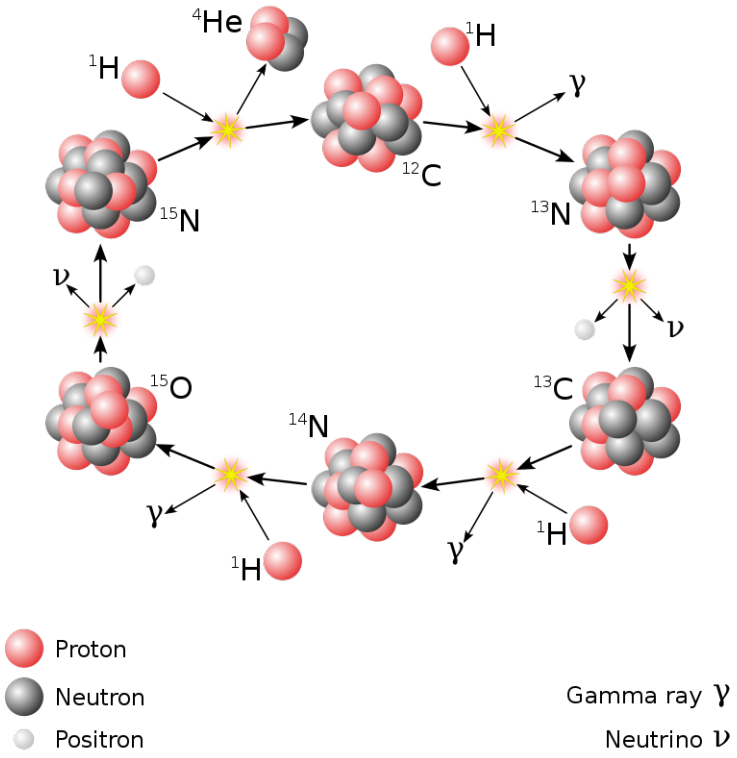

Figure 4: The CNO-Cycle also has significant part in the hydrogen burning processes. It needs C, N and O as Catalysts and a higher temperature (>20 MK) to be dominant, which usually means that it is found predominantly in more massive stars. Starting in the top middle part, ^{12}C gets turned into ^{13}N by proton (red balls) capture with subsequent emission of a γ. By β^+-decay the nucleus turns into ^{13}C by converting a proton into a neutron (grey balls) while emitting a positron (e^+, white balls) and a neutrino (ν). In the same way the nucleus completes a circle through ^{14}N, ^{15}O, ^{15}N and finally back to ^{12}C through means of proton capture (2x), β^+ and then a proton capture-induced α-decay (emitting a ^{4}He nucleus). With this the four captured protons are converted into the ^{4}He nucleus by using the carbon, nitrogen and oxygen nuclei as catalysts. Picture taken from Wikimedia Commons

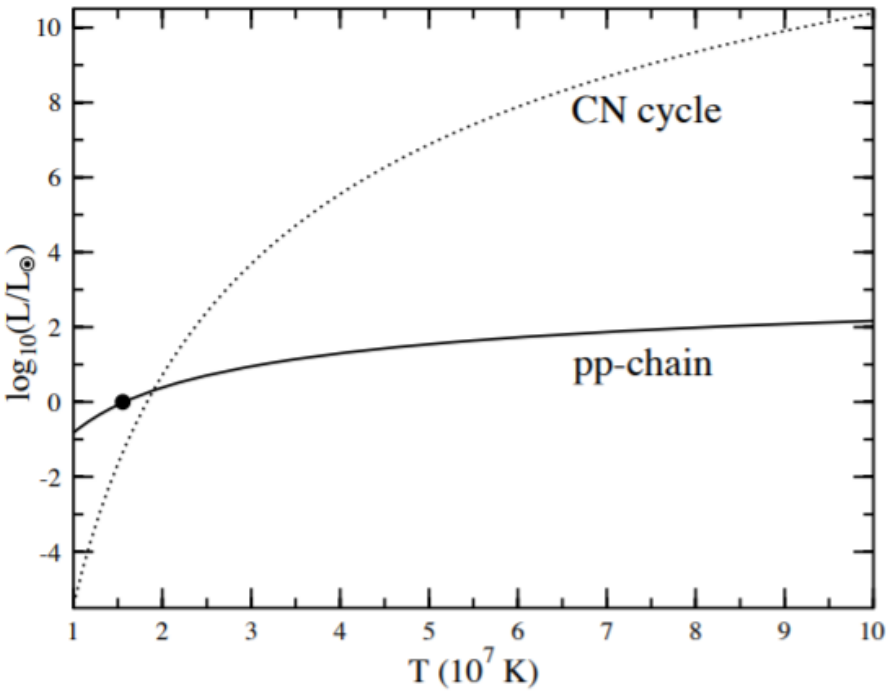

Figure 5: "The stellar energy production as a function of temperature for the pp chain and CN[O] cycle, showing the dominance of the former at solar temperatures. The dot denotes conditions in the solar core: the Sun is powered dominantly by the pp chain.", from fig.1 of Adelberger et al. (2011). For temperatures below around 20 MK the pp-chain is the dominant process in a star, for temperatures above it is the CNO-Cycle. Note that it is possible for both processes to happen even when one of them is dominant.

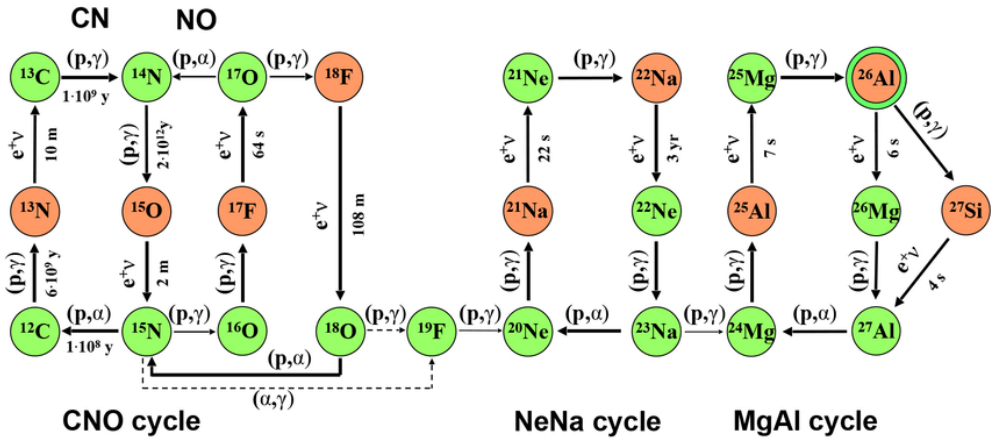

Figure 6: The NeNa and the MgAl Cycles are able to run continuously due to the constant feedback of material from the CNO cycle, from fig.1 of Boeltzig et al. (2016). The procedure is similar to the one of figure 4. ^{1}H of the surroundings is converted into ^{4}He. Notably as well is the production of ^{26}Al, which is therefore replenished in the fusion region despite its radioactive nature.

core, which otherwise would deplete over time due to its radioactive nature. They could also be responsible for abundance anomalies of low-mass stars in globular clusters. The reasoning is that they are polluted by a former population of high-mass stars (able to undergo the CNO-, NeNa- and MgAl-Cycle), so even though the low-mass stars do not undergo the cycles themselves, the products of the processes can still reside in them.

2.1.4 Stellar Structure

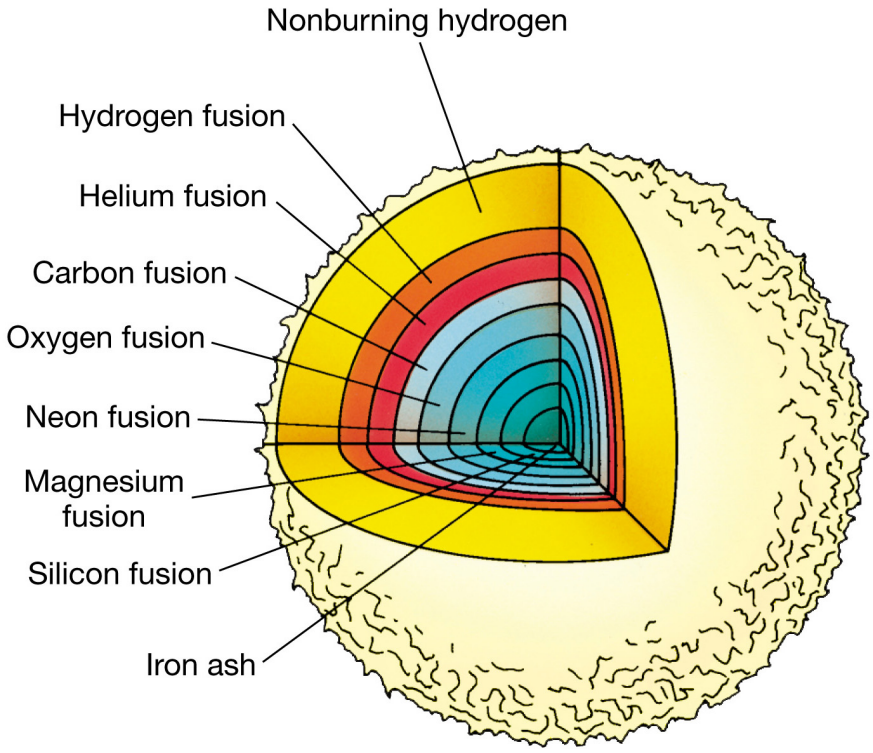

Figure 7: Stars in our vicinity often develop an onion-like structure as the one above. The active fusion material is in the core, whereas the envelope contains material not undergoing fusion itself. In the core the materials are layered depending on their mass. This is a picture after a considerable part of the lifetime of the star has already passed, since silicon fusion has already started. Figure taken from Marti et al. (2021).

Stars near to us usually develop *core-envelope structure* (cf. fig. 7 and Marti et al. 2021). This means that they have a hot core with the actively burning material and a less hot envelope that mostly stays the same composition-wise. The different elements are generally residing in more or less spherically symmetric layers.
Most stars do have such a structure, but there are exceptions: *Chemically homogeneous evolution* (cf. 2.1.5) is a phenomenon that is discussed in the present work and it explicitly deviates from that core-envelope structure.

The radial symmetry of a star mentioned before enables one to approximate a star with a one-dimensional code (cf. 2.2.1).

2.1.5 Differences in Evolutionary Pathways

Although in our local universe the stars generally develop this "onion shell" form, there are different kinds of stars, too: Some stars rotate so quickly that the core-envelope structure is mixed to varying degrees, up to complete mixture. Rotation results in a broken spherical symmetry due to the combined potential of gravity and rotation (and therefore the isobaric layers) being not spherically symmetric (cf. 2.2). This results in material moving along the layers and producing circulation and mixing in the star.
For stars with enhanced mixing the stars can achieve a more or less homogeneous distribution of materials, therefore resulting in the extreme cases *chemically homogeneously evolving* (cf. for example Riley et al. 2021, Yoon & Langer 2005, Brott et al. 2011), which correspondingly gives the form of evolution the name chemically homogeneous evolution (from here on out CHE). Metal-poor environments are favoured for stars with high mass and high rotational velocity. Those stars generally burn through all their material and therefore have a longer lifetime than their same-mass counterparts *evolving normally* (i.e. stars with a core-envelope structure. Their evolutionary pathway is the normal evolution (NE), like those in the higher metallicity environments). Stars undergoing such CHE have a comparably high surface helium mass fraction (similar to the fraction in the core) and evolve to be so-called *Transparent Wind Ultraviolet Intense Stars* (TWUIN stars, cf. Szécsi et al. 2015), which have an optically thin wind and emit intense ionizing radiation.
Additionally there are some stars that exhibit a mixed evolution. Here the stars either start out homogeneously evolving and then due to spin-down lose enough angular momentum to change their evolution into a normal one, or begin their evolution normally evolving and lose their outer layers due to high rotational velocity, leading to the uncovering of more helium-rich layers beneath. This is called *transitional evolution* (TE) (cf. Szécsi et al. 2015). Sign of this behaviour is for example an intermediate surface helium mass fraction (lower than in the core, but higher than the abundances of their original star forming region).

2.1.6 Supergiants

Some stars inflate due to the high luminosity in contrast to their comparably low temperature. Their inside reaches the Eddington limit, facilitating the radiation pressure to overcome the gravity and push the star's outer regions outwards.

This means that the envelope expands considerably, which makes radius and therefore the whole volume of the star bigger. Those stars are considered to be supergiants. Depending on their temperature, those stars can be either called *blue or red supergiants*.
Red (cool) supergiants can take an important part in the development of the populations in globular clusters (GCs), as is discussed in Szécsi & Wünsch (2019) and 1.2, so models of that behaviour are important for their study.

2.2 Modelling

When stars form the aforementioned spherically symmetric shells, a code that is only dependent on the distance to the core (which is one dimension instead of three spacial ones) can reproduce the whole star. This way the computation can be simplified.
There are deviations from this approximation. Stars that rotate very quickly for example flatten due to the centrifugal force (cf. for example Challouf et al. 2017), which breaks the spherical symmetry and creates an oblate shape. In most cases however this deviation can either be neglected or accounted for by additional correction of the data (cf. 2.2.1 last paragraph).

2.2.1 Equations of a One-dimensional Code

There are five partial differential equations which are the backbone for the modelling of stellar evolution (cf. Kippenhahn et al. 2020). The first one concerns the mass distribution. It is expressed by

$$\frac{\partial r}{\partial m} = \frac{1}{4\pi r^2 \rho} \tag{13}$$

with m=$\int_0^r 4\pi r'^2 \rho dr'$ being the *mass coordinate* at a distance r to the centre and ρ the density. It is possible and advantageous to express the equations in terms of this mass coordinate since the mass coordinate is monotonically increasing outwards and simplifies the equations.
The second formula is considering the hydrostatic equilibrium, meaning that it is expressing the balance between the gravitational and the gas- and radiation pressure:

$$\frac{\partial P}{\partial m} = -\frac{Gm}{4\pi r^4} - \frac{1}{4\pi r^2}\frac{\partial^2 r}{\partial t^2} \tag{14}$$

Here G is referring to the gravitational constant and P to the pressure.
In case of hydrostatic equilibrium the time derivative in the second term is equal to 0.

The third equation is arising from the heat balance in the star, therefore satisfying the energy conservation:

$$\frac{\partial L}{\partial m} = \epsilon - T\frac{\partial S}{\partial t} \tag{15}$$

with ϵ referring to the heat source via nuclear processes and the second term to the necessary energy to keep up the heat in the star. This results in the excess energy, which is radiated away, giving the luminosity L.
The transport of energy is cared for with equation 16. It is dependent on the main mode of energy transport in the star.

$$\frac{\partial T}{\partial m} = \frac{T}{P}\frac{\partial P}{\partial m}\nabla \tag{16}$$

Here one then has to insert the correct ∇ corresponding to the main transport method for either mainly radiation or convection, because massive stars have a convective core and a radiative envelope (cf. for example Jin et al. 2015):

$$\nabla_{rad} = \frac{3\kappa LP}{16\pi acT^4 Gm} \tag{17}$$

$$\nabla_{ad} = \left(\frac{\partial \ln(T)}{\partial \ln(P)}\right)_S = \left(1 - \frac{1}{\Gamma}\right) \tag{18}$$

Here a distinction has to be made:
For radiation, which is the transport of energy via photons being radiated away, ∇_{rad} applies. Here the meaning of κ is the Rosseland opacity per unit mass, c is the speed of light and a the radiation constant.
For convection, which is the transport of energy via exchange of hotter and colder mass elements (in this case plasma in the star), ∇_{ad} applies (at least in the deep interior of the massive star), which is defined as the adiabatic temperature gradient and equal to the shown derivative with a constant entropy S. For a more general approach it can be expressed by the efficiency of convection Γ, giving a description of how much influence convection has on the transport of energy.
It is modelled in stellar evolution for example by the application of the mixing-length theory. Here one defines transporting mass elements with a mean free path (called mixing length). After travelling that mixing length, the element dissolves in its surroundings.
Finally when investigating the isotope abundances one needs an equation to regard those changes, giving the last formula:

$$\frac{\partial X_i}{\partial t} = \frac{m_i}{\rho}(-\Sigma_{j,k} r_{i,j,k} + \Sigma_{k,l} r_{k,l,i}) \tag{19}$$

Here the isotope abundance of a given isotope $X_i = \frac{m_i n_i}{\rho}$ changes depending on the reaction rates r from reactions both creating from and destroying into other isotopes.

Results of Spherical Symmetry Breaking due to Rotation

As stated in the beginning of paragraph 2.2 the spherical symmetry breaks due to rotation. To still use a one-dimensional code some corrections are needed, which will shortly be summarized here:

Instead of expressing the model by means of spherical shells with radius r, one uses spheres of constant pressure with radius r_P, mass m_P and Volume V_P. For such spheres one gets accordingly $\frac{\partial r_P}{\partial m_P} = \frac{1}{4\pi r_P^2 \rho}$.

For quantities not constant over the surface S_P of those isobaric spheres a mean value $\langle \cdot \rangle$ is defined by integrating over and dividing by the absolute value of the constant surface S_P.

With this one gets for the second equation $\frac{\partial P}{\partial m_P} = -\frac{G m_P}{4\pi r_P^4} f_P - \frac{1}{4\pi r_P^2} \frac{\partial^2 r_P}{\partial t^2}$ with $f_P = \frac{4\pi r_P^4}{G\, m_P\, S_P} \langle g^{-1} \rangle^{-1}$, where $g = |\boldsymbol{g}|$ the *effective* gravitational acceleration, combining gravitational and rotational effects.

For the radiative temperature gradient one gets:
$\frac{\partial T}{\partial m} = \frac{f_T}{f_P} \frac{3\kappa L_P P}{16\pi a c T^4 G m_P} \left[1 + \frac{r_P^2}{G\, m_P\, f_P} \left(\frac{\partial^2 r_P}{\partial t^2}\right)\right]^{-1}$ with $f_T = \left(\frac{4\pi r_P^2}{S_P}\right)^2 (\langle g \rangle \langle g^{-1} \rangle)^{-1}$ and L_P the flux through S_P (cf. Heger et al. 2000, Endal & Sofia 1976).

The similar structure of those new equations makes it easy to implement them in place of the old ones without much change. They facilitate the continued use of a one-dimensional code for modelling despite the rotational influence on the shape of the star.

2.2.2 Bonn-Code

The *Bonn-Code* (also known as Binary Evolutionary Code or short BEC) is written in Fortran and can model evolution of single and binary stars.

The user provides initial parameters for the code that get assigned to the best fitting initial model already saved. Afterwards a copy of that model is altered to completely fit the parameters given. This is the initialisation process and is not considered to be part of the time progression. For each step of that process, the corresponding physical properties of the model are determined with the equations mentioned in the subsection before (cf. 2.2.1).

After the initialisation is complete, the real time evolution starts. The code computes the physical quantities and their change for each time step. It chooses the length on its own in a sensible way, depending on the processes active. After each time step a new static model is created based on the model of the last time point,

which produces a model evolution sequence over time (cf. Suijs 2006).
How often the models are actually saved can then be controlled via parameters. This is done to keep the data load comparably small. Instead of saving every model the code keeps only some (cf. 2.2.3), which are compressed in the binary file format.
With this procedure one gets model sequences that have data of all physical properties for the whole evolution.

2.2.3 Parameters and Physical Properties

0	1	0.000000000E+1	9.9E+7	9.0000
100	2	0.000000000E+1	1.1E+8	10.0000
101	3	0.000000000E+1	9.8E+8	10.0000
102	4	0.000000000E+1	9.8E+8	10.0000
104	5	3.168808932E+3	2.6E+3	10.0000
150	6	2.974209094E+4	2.6E+2	10.0000
200	7	1.386974544E+5	2.0E+4	10.0000
250	8	4.500202843E+6	8.3E+4	9.9998
300	9	8.075362320E+6	6.1E+4	9.9997
350	10	1.070061915E+7	4.5E+4	9.9995
400	11	1.265284594E+7	3.4E+4	9.9994
450	12	1.413299447E+7	2.6E+4	9.9992
500	13	1.527202687E+7	2.0E+4	9.9991
550	14	1.614878643E+7	1.5E+4	9.9990
555	15	1.622482318E+7	1.5E+4	9.9990
#1 MODEL	NR	t	DTN	GMS

Figure 8: A model sequence (initially 10 $M_{\odot}$), depicting the evolution in each saved step (NR, cf. 2.2.3). One can see the time since the initialisation in column 3 (t in yrs), the length of the time steps in column 4 (DTN in yrs) and the mass in column 5 (GMS in $M_{\odot}$). Also shown is the index number of every run depicted in the first column (MODEL) and the index number of each time another model is actually saved in the files, which is used to decrease the amount of data, in column 2 (NR).

The stars are characterized by various parameters.
Inputs for the Bonn-Code models are initial mass M_{ini} (which can range from sub-solar to multiple hundreds of solar mass), initial metallicity Z_{ini} (abundance ratios of materials heavier than helium (cf. 2.1.1), which can range from around milky way metallicity to a fraction of that of for example the small magellanic cloud) and initial rotational velocity $v_{rot,ini}$.
Those three parameters are supervised further in the progression of the evolution; stars typically lose some mass while evolving, they can either spin up due to

contraction or spin down due to loss of angular momentum via massloss, and the composition of the various isotopes (at surface, core and the points in-between) also changes over time because of the nuclear processes.
Other physical properties are supervised as well. Temperature of the surface, luminosity, radius, rotational velocity and various isotope abundances can be called upon by extracting the data from the files.
Furthermore the models are characterized by some important *Code-parameters* to for example change resolution or run-length.
Noteworthy here are the following (cf. fig. 8):
The time passed since initialisation is saved in t, the length of the time step in DTN (both in units of years).
MAXZAL sets the number of steps the code does until stopping the evolution. With changing this one can achieve a higher amount of steps (MODEL, see next paragraph) until stopping.
MODEL is the number of the current step. It is a value that is increased for each model in the sequence and goes up to roughly the value of MAXZAL.
The MODEL number is divided into different sections with NR. This is done so that the amount of data stored does not become overwhelming. Only the models starting a new entry in NR are completely saved in the files (meaning that the physical properties of every point computed in the interior is saved), the other models only in parts (i.e. core and surface properties, but not the progression in-between).
One can set the step width until a new NR section with the parameters IOUT and IPRN, therefore achieving a finer or broader resolution of the files depending on the needs. This can also be changed while already running the evolution, so that different parts of the evolutionary process can be resolved differently.

2.2.4 BoOST-Format

When saving the data, one can be faced with the problem of too big amounts of data for comparably very little benefit. Therefore it can be useful to create data formats that still retain the general information while still being compressed.
Additionally creating such a format can have the benefit of compatibility with other programs using the data (like for example SILCC (cf. Walch et al. 2015 and 1.1)).
The BoOST-format (cf. Szécsi et al. 2022 and 1.1) facilitates the compression of the amounts of output data of the Bonn-Code to a form that fits both criteria. In figure 9, where diagrams of "unboosted" and "boosted" stellar evolution tracks are depicted (cf. next section), it is shown that one retains the general form of the data while losing (for some appliances) unnecessary data.

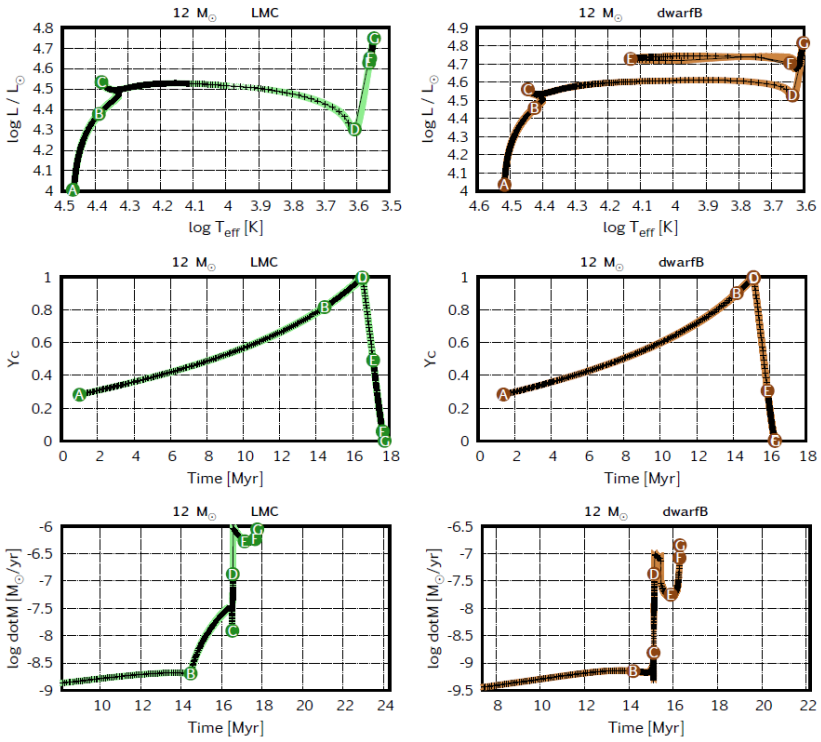

Figure 9: Hertzsprung-Russell (top), core helium abundance (middle) and mass-loss (logarithmic) diagrams of two models ($M_{ini} = 12\,M_{\odot}$, $v_{rot,ini} = 100\,km/s$, $Z_{ini} = Z_{LMC}$ and $Z_{ini} = 0.2\,Z_{SMC}$ respectively) with data points of a boosted model (black crosses) over the data of an unboosted model (green/brown line). The models are chosen to be comparable to figure 2. By comparing them one can see that the general shape is conserved, but especially in the Hertzsprung gap a considerable amount of unnecessary data is filtered out. Furthermore the equivalent evolutionary phases (EEPs) are pointed out in the figures to show why they were defined in this way. They help ensuring that enough data is conserved in each phase to still be representable when applying the boost format. Figure taken from Szécsi et al. (2022).

To achieve this so-called *"equivalent evolutionary phases" (EEPs)* are introduced to facilitate the separation of the evolution in sensible parts, so that only data is removed that is not necessary to retain the essential information. While they are also marked in figure 9, they shall be quickly discussed in the following paragraph:

EEPs

The first EEP (A) is the phase from the beginning of the model (after the initial hook phase, cf. section 2 Models, Initialisation phase) until a point of either a "local minimum of the mass loss rate corresponding to the bi-stability jump" (cf. Szécsi et al. 2022) or (if this does not happen in the main phase) of around 75% of the main sequence lifetime.

From that point up till either the tip of the hook at the end of the main sequence

or (if this hook is not visible) to the point close to core-hydrogen-exhaustion the second EEP (B) is defined.
There is a total of seven EEPs for the lifetime of stars up till core-helium-exhaustion ($Y_C = 0.0$, End of EEP G), and for each the BoOST format stipulates a fixed number of data lines.
The other phases are not that important for the following work since the models right now only cover parts of the main sequence.

3 The Models

For the present work 336 Models were created with the Bonn-Code. They differed in initial mass (ranging from 10 to 500 $M_\odot$), initial metallicity (ranging from milky way metallicity to 2% of the metallicity of the small magellanic cloud) and initial rotational velocity (ranging from 0 to 500 km/s).
The complete set of chosen parameters is depicted in table 2.

Init. mass (in $M_\odot$)	10	20	40	80	150	300	500	
Init. vel. (in km/s)	0	100	200	300	400	500		
Init. met. (in Z_{SMC})	5	2	1	0.5	0.2	0.1	0.05	0.02
	$\widehat{=}Z_{MW}$	$\widehat{=}Z_{LMC}$						

Table 2: Chosen initial parameter set used for the models. The masses are roughly equidistant on a logarithmic scale, the velocities are multiples of 100 km/s and the metallicities are sets of 1, 0.5 and 0.2 times multiple powers of 10 (cf. 3).

The initial rotational velocity was chosen in 100 km/s steps.
The chosen initial metallicities were sets of 1, 0.5 and 0.2 times 10^{-n} of the metallicity of the small magellanic cloud (SMC, with Z_{SMC}), additionally to the regular metallicity of the milky way (MW, with $Z_{MW} = 5 \cdot Z_{SMC}$) and the large magellanic cloud (LMC, with $Z_{LMC} = 2 \cdot Z_{SMC}$). This is also presented in figure 10 in a logarithmic scale.
These metallicities explicitly include that of the dwarf galaxy I Zw 18 (cf. 1.1),

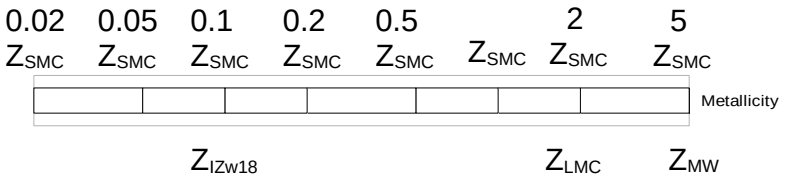

Figure 10: The used initial metallicities of the models created for this thesis, shown on a logarithmic scale. They include those of the milky way, the large and the small magellanic cloud and go down to a fraction of 0.02 Z_{SMC}.

which is $Z_{ini} = 0.02\, Z_{MW} = 0.1\, Z_{SMC}$. It is used in multiple sources relied on in this work to enable a comparison and future enhancement (cf. for example Szécsi et al. 2015, Szécsi & Wünsch 2019 and Szécsi et al. 2022).
For the initial masses the values were set manually because they were semi-arbitrarily chosen without a fixed rule to determine them. The main criterion

was for them to be about equidistant on a logarithmic scale.
When starting the code the models first were initialized, which creates a first model at the beginning of the main sequence. A homogeneous mass in hydrostatic and thermal equilibrium with the set initial parameters is created that then undergoes some changes; the stars change to a core-envelope structure, they contract (and therefore increase their surface rotational velocity) and change the temperature (the core temperature increasing more than the surface), until a point of $Y_C = 0.28$ is reached, which we define as the ZAMS (cf. 2.1.2 and Szécsi et al. 2015).
After that initialisation phase the code started with the regular time evolution. The models were set to run until a point of around $Y_C = 0.6$ was reached. This was chosen deliberately, because it is short of the second EEP in the BoOST format, which the models are planned to eventually be converted into. Stopping short of that points facilitates smaller saved steps and therefore finer resolution in the areas of change in the future.
Additionally when nearing the end of the main sequence, the topic of lithium production and destruction gets more and more relevant (cf. 2.1.3 and Sackmann & Boothroyd 1998), which leads to the consideration of finer resolution in that regard as well.
With this the models generally reach around 60% of the main sequence. This is only an approximation, as the models are initialized already with some kind of amount of helium in the core from the beginning (This is as intended, because the gas that creates the stars in reality is usually composed of around 75% hydrogen and 24% helium (between primordial (cf. Peimbert et al. 2007) and solar (cf. Grevesse et al. 1996))).
To achieve this a first run of those models was done with a big MAXZAL value. With those it was possible to determine the model number MODEL where it will reach $Y_C = 0.6$, which was then used as the new MAXZAL value for a new run. Also the steps in which a model snapshot was saved to a new NR was set with IOUT and IPRN=50. With this, every 50th model was saved in a new NR entry. Not all Models reached that stage of $Y_C = 0.6$. For a few (in the area of high initial masses, high initial metallicity and high initial velocity, cf. fig. 15, top left corner) the default settings of the code could not reach a converging solution. This is because those stars are physically too close to the Eddington limit and therefore challenging to numerically find solutions (cf. Agrawal, Stevenson, et al. 2021, Agrawal, Szécsi, et al. 2021). It is a goal for the future to challenge these problematic cases.

3.1 The Diagrams

There are a few diagrams that are often used to visualize stars, which will be discussed here to ease the discussion later on.

3.1.1 Hertzsprung-Russell Diagram

The plot in figure 11 is a *Hertzsprung-Russell diagram* (HRD). It depicts the luminosity of a given star (in $L_\odot$ and a logarithmic scale) vs. the temperature (in K, a logarithmic scale and with an inverse direction of growing, meaning that hotter stars are more to the left than cooler ones, for historical reasons).
These plots can be used to give both observations and theoretical models a context. One can compare different positions in the HRD plot to see that one star is hotter or more luminous than the other.

Additionally one can use a HRD to visualise the evolutionary track of a stellar model (cf. fig. 9). It is a popular choice of visualization, because the luminosity, temperature and mass have a close connection, which means that depicting stars like this gives information about the state of a star. It also possibly gives additional information about quantities like the radius of the star via the Stefan-Boltzmann law or the evolutionary stage by comparison to former or latter stages.

3.1.2 Various Physical Properties over Time

Another useful way to display information gained from the models is a plot of some property over time.
One can see the exact development over time of this property, which enables the reader to recognize characteristic features of the evolution.

In figure 12 an example of such a diagram is shown. The helium mass fraction at the surface is depicted for models with $M_{ini} = 500\,M_\odot$, $Z_{ini} = 0.5\,Z_{SMC}$ and various initial rotational velocities.
In contrast to for example the HRD, it is also useful to compare different phases time-wise. If one saw two phases of an evolution in a HRD, one would not be able to discern the lengths of those phases, unless one also applies some kind of marker for time steps (e.g. isochrone dots, as in fig. 2).
There are many properties where this can be useful, some of them being the composition fraction of selected nuclei, mass or massloss or the radius.

3.1.3 Abundance Plots

Another way to depict the data is by means of the *abundance plots* (cf. fig. 13). Here the abundances of various isotopes are depicted vs. the mass-coordinate (cf.

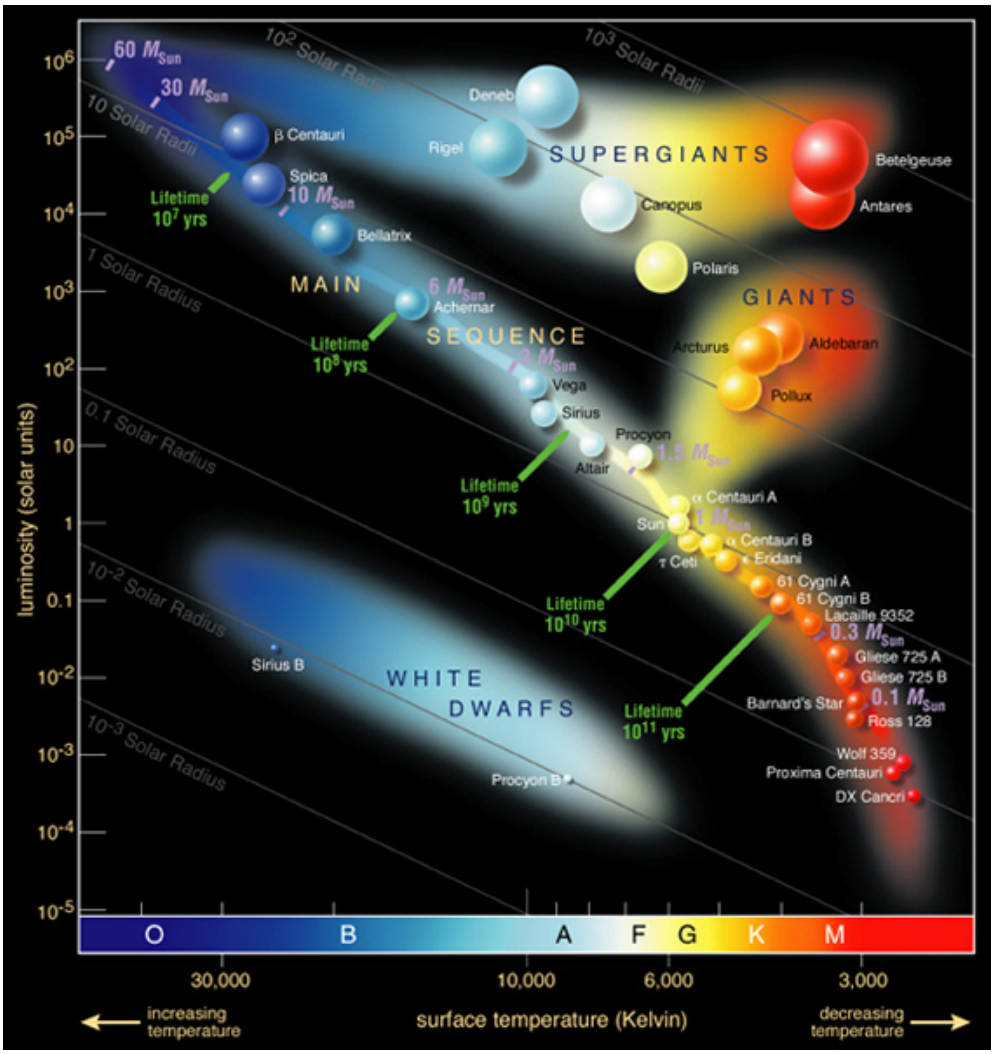

Figure 11: The Hertzsprung-Russell diagram (HRD) can be used to show stars position with respect to their luminosity and temperature. The luminosity is depicted (in $L_\odot$ and a logarithmic scale) against the surface temperature (in K, with a logarithmic and inverted scale). Additionally spectral types according to the temperature are marked. Various observed stars are shown (with their masses) at their position in the HRD, showing the main sequence (inhabited by stars that undergo hydrogen burning), giant (inhabited by helium burning stars), supergiant (inhabited by massive helium burning and by massive cool hydrogen burning stars, cf. 2.1.6) and white dwarf area (inhabited by stars that do not have enough mass and therefore cannot reach a high enough temperature to ignite more advanced fusion processes). Figure taken from Cesar (2021)

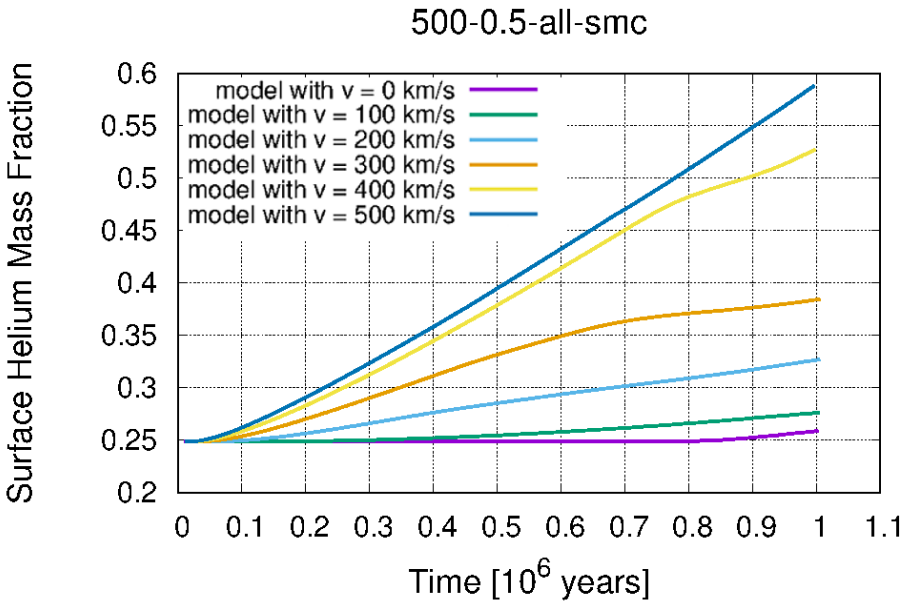

Figure 12: An example for the development over time plot. Here the surface helium mass fraction is depicted for models with $M_{ini} = 500\,M_{\odot}$, $Z_{ini} = 0.5\,Z_{SMC}$ and various initial rotational velocities. One can see that the high velocities (dark blue, yellow line) reach higher surface helium mass fractions than lower velocities (purple line).

2.2.1), to for example show the progression of mixing through the star. One can see the core/envelope structure by means of the crossing point, until which the hydrogen decreases and the helium increases (cf. fig. 27 in a later section 4.5). For stars where no such structure (or only parts of it) exists one cannot see this crossing point (cf. fig. 28) or it will be close to the surface (high mass-coordinate, cf. fig. 29).
One can also supervise the development of isotope abundances of for example Mg and Al or Ne and Na to investigate on the MgAl- and NeNa-Cycle, or of lithium to investigate the increased lithium abundances in some low-mass stars (not in fig. 13).

3.1.4 Surface Helium Mass Fraction

Another plot that is interesting is that of the helium mass fraction at the surface of a given stellar model (cf. fig. 14).
It can be plotted against initial mass, initial velocity, initial metallicity or any other physical property, which then lets the reader compare different configurations against each other.
The helium mass fraction at the surface is only one example, other properties can be chosen as well. The helium mass fraction at the surface for example can

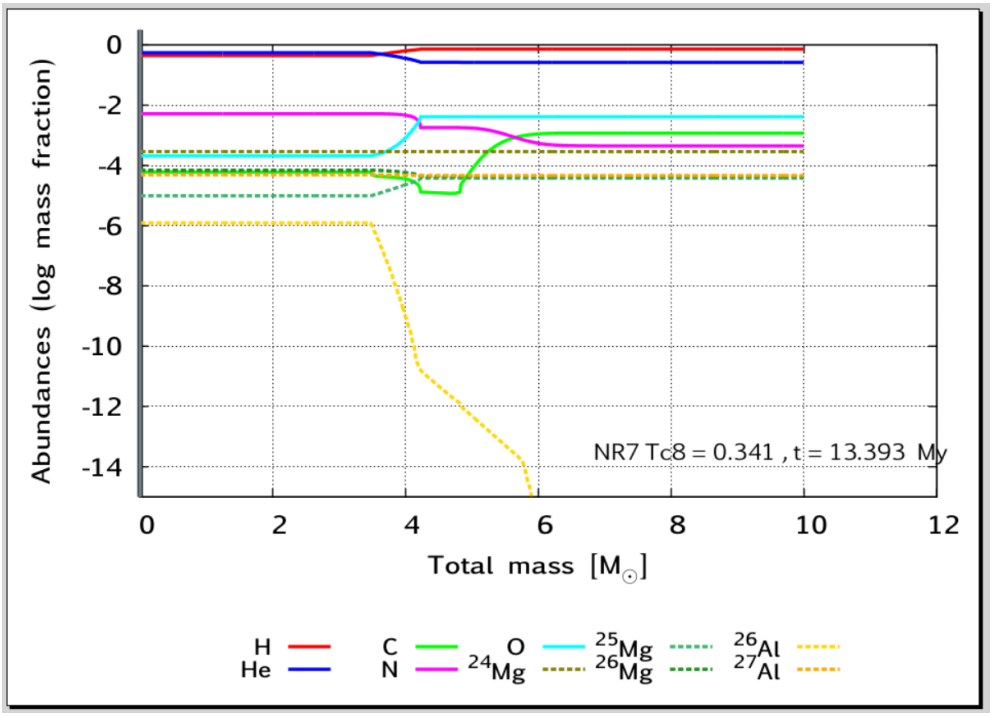

Figure 13: An example for the abundance plots. The abundances of various isotopes and elements (hydrogen, helium, carbon, neon, oxygen, magnesium (^{24}Mg, ^{25}Mg, ^{26}Mg), aluminium (^{26}Al, ^{27}Al)) with respect to the mass coordinate (cf. 2.2.1) in units of $M_\odot$ at a given time (t=13.393 $Myrs$) for a model with $M_{ini} = 10\,M_\odot$, $Z_{ini} = Z_{MW}$ and no initial rotational velocity. One can see that up till around $4\,M_\odot$ the abundances are about constant throughout the star, which is because this is the core, where the isotopes are steadily produced through fusion processes. Above that limit for example the ^{26}Al abundance drops due to its radioactive nature. Here the envelope is not taking part in the fusion processes, which facilitates different abundance ratios.

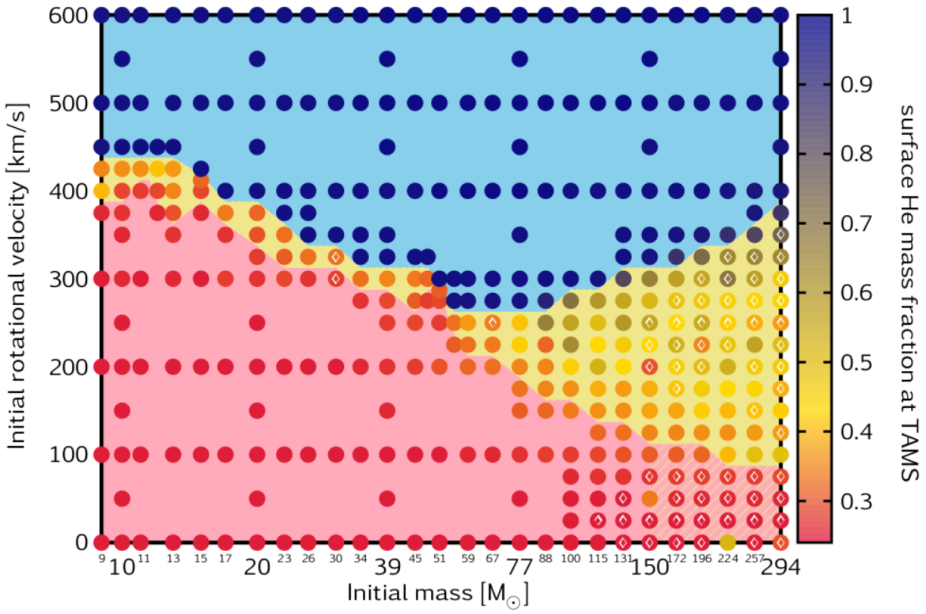

Figure 14: With this diagram one can depict the helium mass fraction at the surface (colour coded) for multiple models in dependency of various input parameters like for example here initial mass (x-axis) and initial velocity (y-axis). A high mass fraction of helium is marked with blue colours, a low one with red and intermediate fractions with yellow. Each dot represents one model sequence at the end of the main sequence. The diagram is also sectioned into different areas of similar colour, which indicates a similar evolutionary pathway (cf. 2.1.4), and the transitions between those areas are more closely resolved (more models created in that area of the parameter space). Some models were not finished until the end of the main sequence, those are indicated by the diamond shapes in the dots. This also results in an uncertainty in the separation line between the red and yellow area, which is indicated by the red area with yellow dashes. Figure taken from Szécsi et al. (2015)

be used to determine if a star underwent NE or CHE, because when undergoing CHE the surface helium mass fraction at the end of the main sequence is close to 1, whereas for normally evolving models it should still be roughly the same as in the beginning of the evolution.

3.1.5 Bulkplots

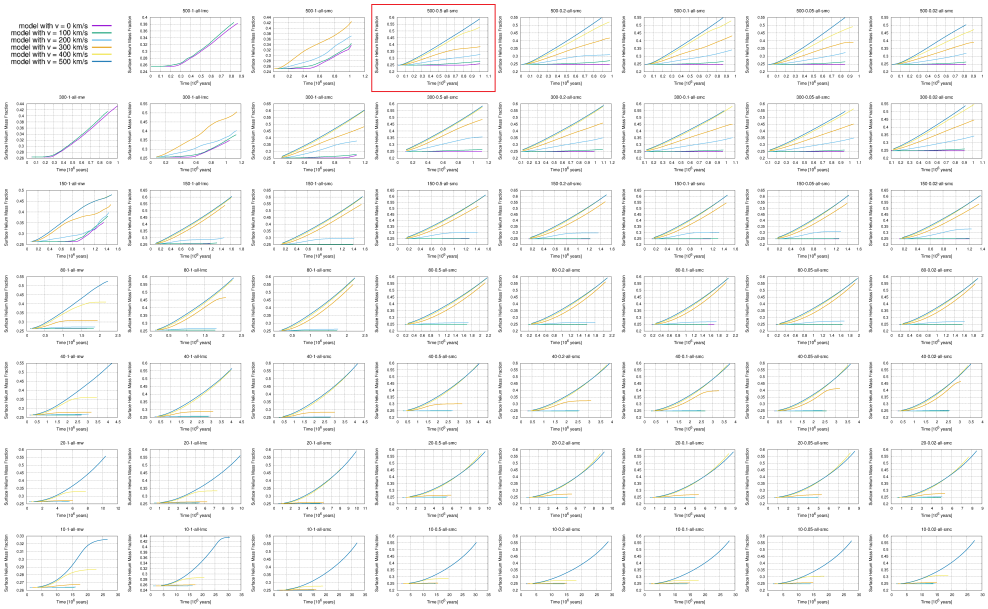

Figure 15: The format of a bulkplot is beneficial to survey the big amount of models in a comparing way. From top to bottom the initial masses of the models decrease (from 500 to 10 $M_\odot$) and from left to right the initial metallicity decreases (from Z_{MW} to $0.02\,Z_{SMC}$). The key for the initial rotational velocity lines is in the top left. The red rectangle marks the cutout that is depicted in figure 12. The complete figure is depicted in landscape format in figure 24.

As this work handles a big grid of input parameters, it is useful to create so-called *bulkplots*. Those plots depict the diagrams of a chosen dependency with additional respect to the free input parameters (initial mass, initial metallicity and initial rotational velocity). In figure 15 such a bulkplot (here for the surface helium mass fraction vs. time plots) is depicted, which is explained here for future convenience.
The plots are ordered as following:
From left to right there are decreasing initial metallicities, starting from $Z_{ini} = Z_{MW}$ to $Z_{ini} = 0.02\,Z_{SMC}$. From top to bottom there are decreasing initial masses, starting from $M_{ini} = 500\,M_\odot$ to $M_{ini} = 10\,M_\odot$.
In each diagram there are all graphs for varying initial rotational velocities in different colours depicted, ranging from $v_{rot,ini} = 0\,km/s$ (purple) to $v_{rot,ini} = 500\,km/s$ (dark blue). In the top left corner of the bulkplot one can also find

a key for the different colours. The red rectangle indicates a cutout, shown in figure 12.
This format is useful to compare evolutionary models. One can either keep the scales fixed to see absolute variations in the plots or possibly keep the scales flexible to facilitate a better comparison between the different velocity graphs.

4 Results

All bulkplots depicted in this section are also shown in Appendix A.2 without caption to provide them in a zoomed-in fashion. They are also in a high resolution, which makes it possible for readers on the computer to zoom in manually.

4.1 Core Helium Mass Fraction

In figure 16 and an exemplary cutout in figure 17 one can see the Core Helium Mass Fraction against the time. As this was the determining factor in the termination of the runs, one can see how the models progressed towards that goal.
One can see in the diagram by comparing the graphs that the models usually reach the set end point of $Y_C = 0.6$. However, there are some differences:
One aspect is the time, in which the models evolve. In the figure one can see that the more massive stars develop more slowly than the lighter ones, the former reaching $Y_C = 0.6$ at around $10^6\,yrs$ ($500\,M_\odot$), whereas the latter taking up to $10^7\,yrs$ ($10\,M_\odot$).
Another thing observable is that there are differences for varying initial rotational velocities. Stars with higher ones tend to develop slower, as can be seen in the 500 and $400\,km/s$ lines (dark blue and yellow), which are the lowest lines in each graph and have the flattest slope.
Both results were to be expected:
In Harwit (2006) (in Fig 8.1) and Kuiper (1938) it can be seen that more massive stars have a higher luminosity output (cf. Mass-Luminosity relation $\frac{L}{L_\odot} \sim \left(\frac{M}{M_\odot}\right)^\alpha$ with $3 \leq \alpha \leq 6$, Kippenhahn et al. 2020) and therefore tend to have a less long lifetime, resulting in faster reaching the depletion of fusion material (cf. for example LoPresto 2018 using $\alpha = 3.5$ with the relation $t \sim M/M^{3.5} = M^{-2.5}$, and also the isochrone dot representation of the HRD in subsection 4.3).
In contrast to that higher initial rotational velocity increases the lifetime of the models, because with rotation more mixing of the material is present, which for same initial masses results in higher mass of material available for fusion processes.
This effect is highlighted especially by the models undergoing CHE (cf. 2.1.4), for example the $v = 400$ or $500\,km/s$ lines of $M = 10$ and $20\,M_\odot$. Here the complete mass of the model is mixed, which results in a longer lifetime.

4.2 Mass and Massloss

In figure 18 a bulkplot for the development of the mass over time is depicted.
The mass is steadily declining because of radiation- and rotation-driven massloss.

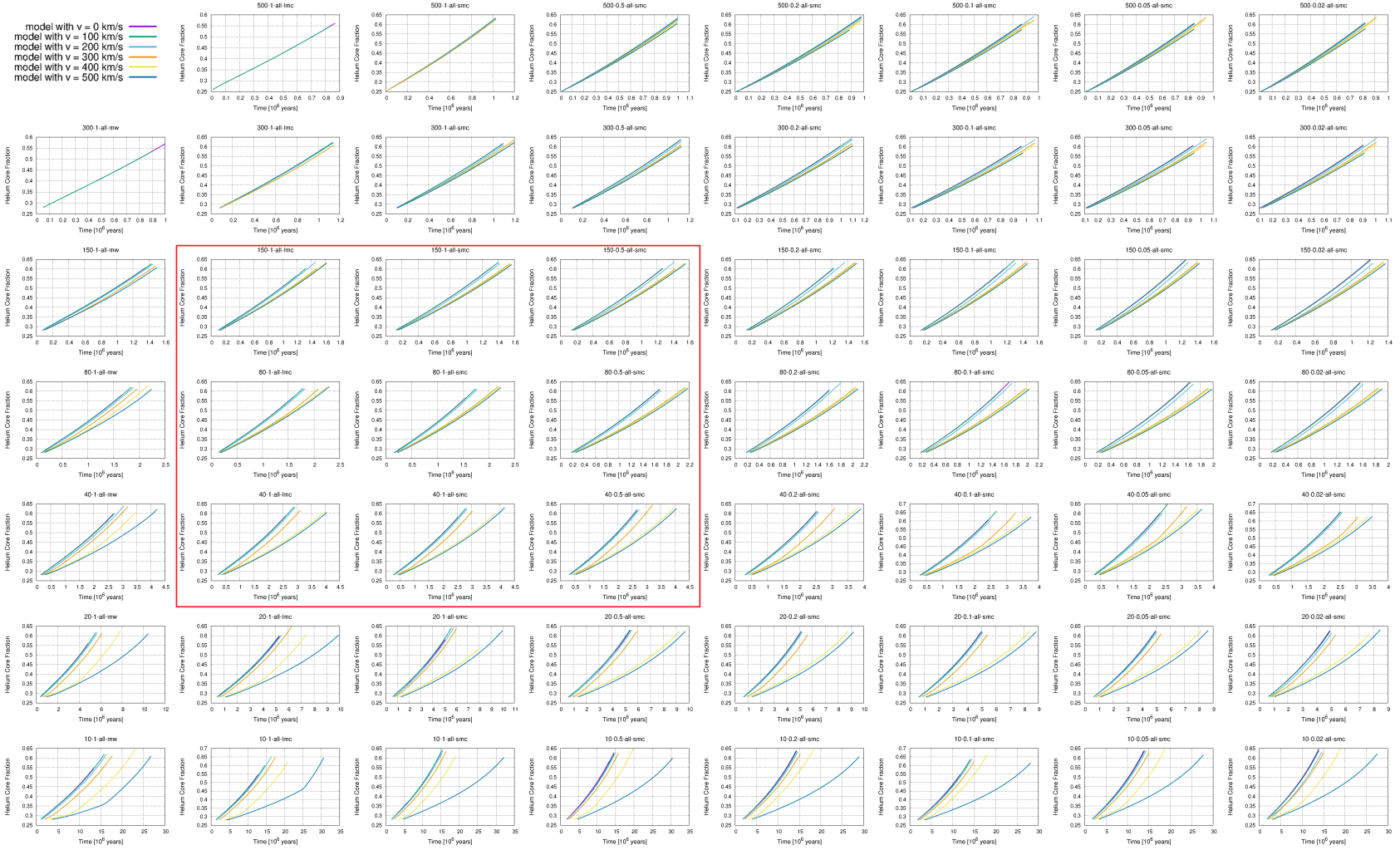

Figure 16: The bulkplot (cf. fig. 15) for the core helium mass fraction of the model sequences over time. The bulkplot format presents all sequences in a grid: Initial masses are ordered from the top ($M_{ini} = 500\,M_{\odot}$) to the bottom ($M_{ini} = 10\,M_{\odot}$), initial metallicities from left ($Z_{ini} = Z_{MW}$) to right ($Z_{ini} = 0.02\,Z_{SMC}$). Each point in the grid shows the graphs for all the initial rotational velocities of that given parameter setting, from $v_{ini} = 500\,km/s$ (dark blue line) down to $v_{ini} = 0\,km/s$ (purple line). The red rectangle indicates the area which is shown again zoomed-in in figure 17. In this bulkplot the core helium mass fraction of the model sequences is plotted against the time in $10^6\,yrs$. In this way the progression of the hydrogen fusion process in those models is shown. The longer the sequences have undergone the hydrogen fusion, the higher the helium abundance in the core becomes. This facilitates the comparison of multiple sequences with regard to their lifetime and the speed with which they move through the main sequence. It is shown that more massive models evolve quicker and reach the end of the sequence faster than the less massive ones. Additionally one can see that a higher initial rotational velocity leads to a slower evolution as well.

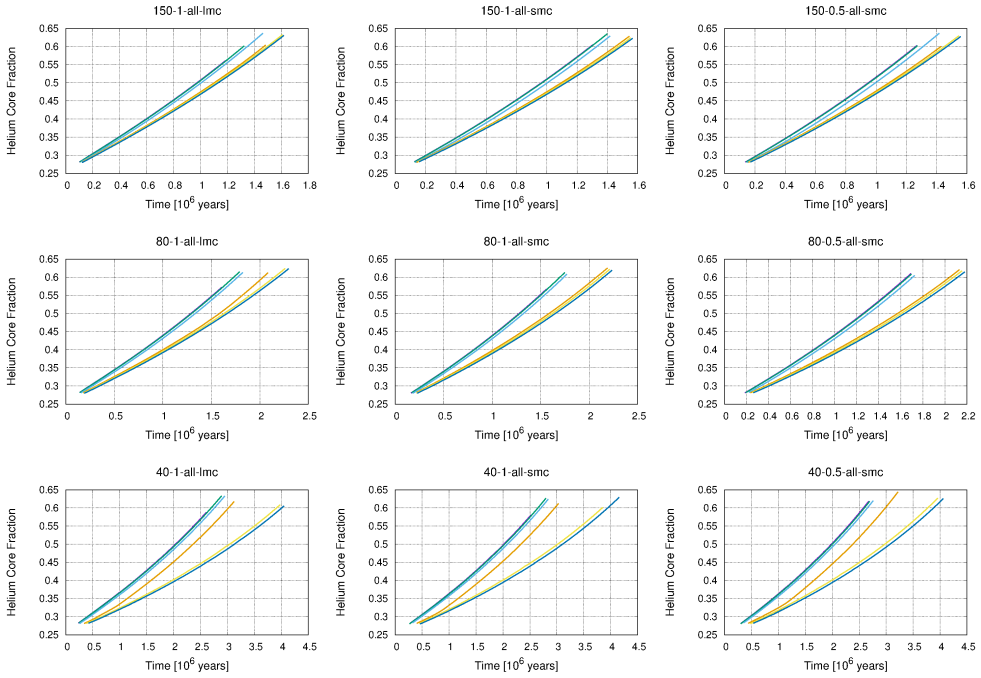

Figure 17: Exemplary cutout of the core helium mass fraction bulkplot (cf. 3.1.5 and caption of fig. 16) for better accessibility. Shown here is the area of $M_{ini} =$ 150 to 40 $M_{\odot}$ and $Z_{ini} = Z_{LMC}$ to 0.5 Z_{SMC}. One can see the difference in time it takes for the sequences to reach the end ($Y_C = 0.6$) depending on the initial rotational velocity (higher velocities leading to slower evolution) and initial mass (higher masses leading to faster evolution).

Figure 18: The bulkplot (cf. 3.1.5 and caption of fig. 16) for the mass of the models (in $M_\odot$) over time (in $10^6\,yrs$) with a fixed mass scale and a flexible time scale. The red rectangle indicates the area which is shown again in figure 19. The lines are declining over time due to massloss, depending on the initial parameter set (cf. eq. 20). Higher initial masses and initial metallicities lead to increased massloss.

Notable here is that there is a difference in massloss if one compares models with differing initial mass or initial metallicity:

A good example for that is the area of $M = 300$ to $80\,M_\odot$ and of $Z = Z_{MW}$

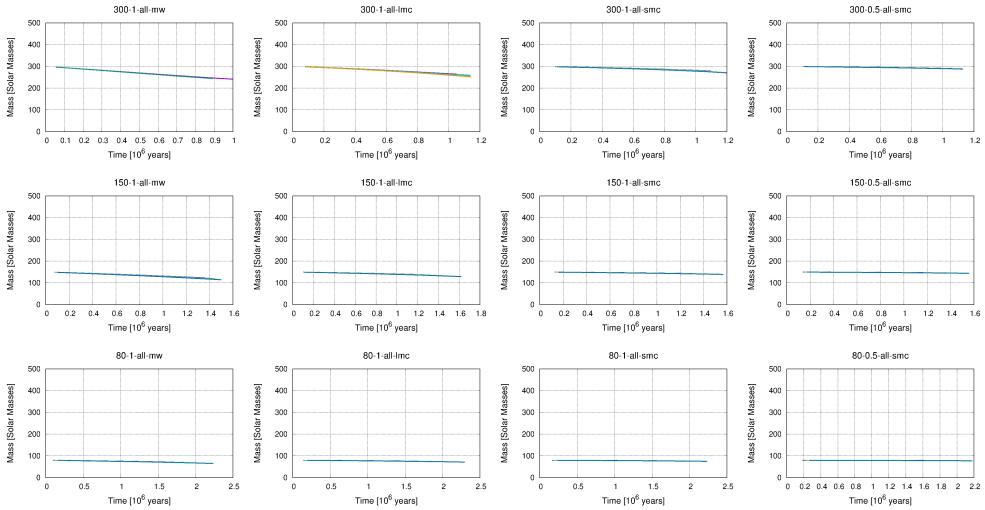

Figure 19: Exemplary cutout of the bulkplot (cf. 3.1.5 and caption of fig. 16) for the mass of the models (in $M_\odot$) over time (in $10^6\,yrs$) with a flexible mass and time scale (cf. fig. 18), fixed on $M_{ini} = 300$ to $80\,M_\odot$ and $Z_{ini} = Z_{MW}$ to $0.5 \cdot Z_{SMC}$. In this cutout the differences between various initial masses and metallicities are shown. Higher ones lead to an increased massloss.

to $0.5 \cdot Z_{SMC}$, a zoom-in of which is shown in figure 19. Here one can see that for higher initial masses and for higher initial metallicity the slope is much steeper, indicating an increased massloss for those parameters. This is not surprising considering the used mass formula for the relevant temperature range ($27500\,K \leq T_{surf} \leq 50000\,K$) from Vink et al. 2001:

$$\begin{aligned} log\dot{M} = &-6.697(\pm 0.061) \\ &+2.194(\pm 0.021)\log(L/10^5\,L_\odot) \\ &-1.313(\pm 0.046)\log(M/30M_\odot) \\ &-1.226(\pm 0.037)\log\frac{v_\infty/v_{esc}}{2.0} \\ &+0.933(\pm 0.064)\log(T_{surf}/40000\,K) \\ &-10.92(\pm 0.90)\,(\log(Teff/40000\,K))^2 \\ &+0.85(\pm 0.10)\log(Z/Z_\odot) \end{aligned} \tag{20}$$

The massloss increases for higher masses and metallicities (cf. also Vink et al. 2000 and Vink & Sander 2021). Additionally, there is a dependency of the initial rotational velocity, as can be seen in figure 20. Here the same bulkplot was

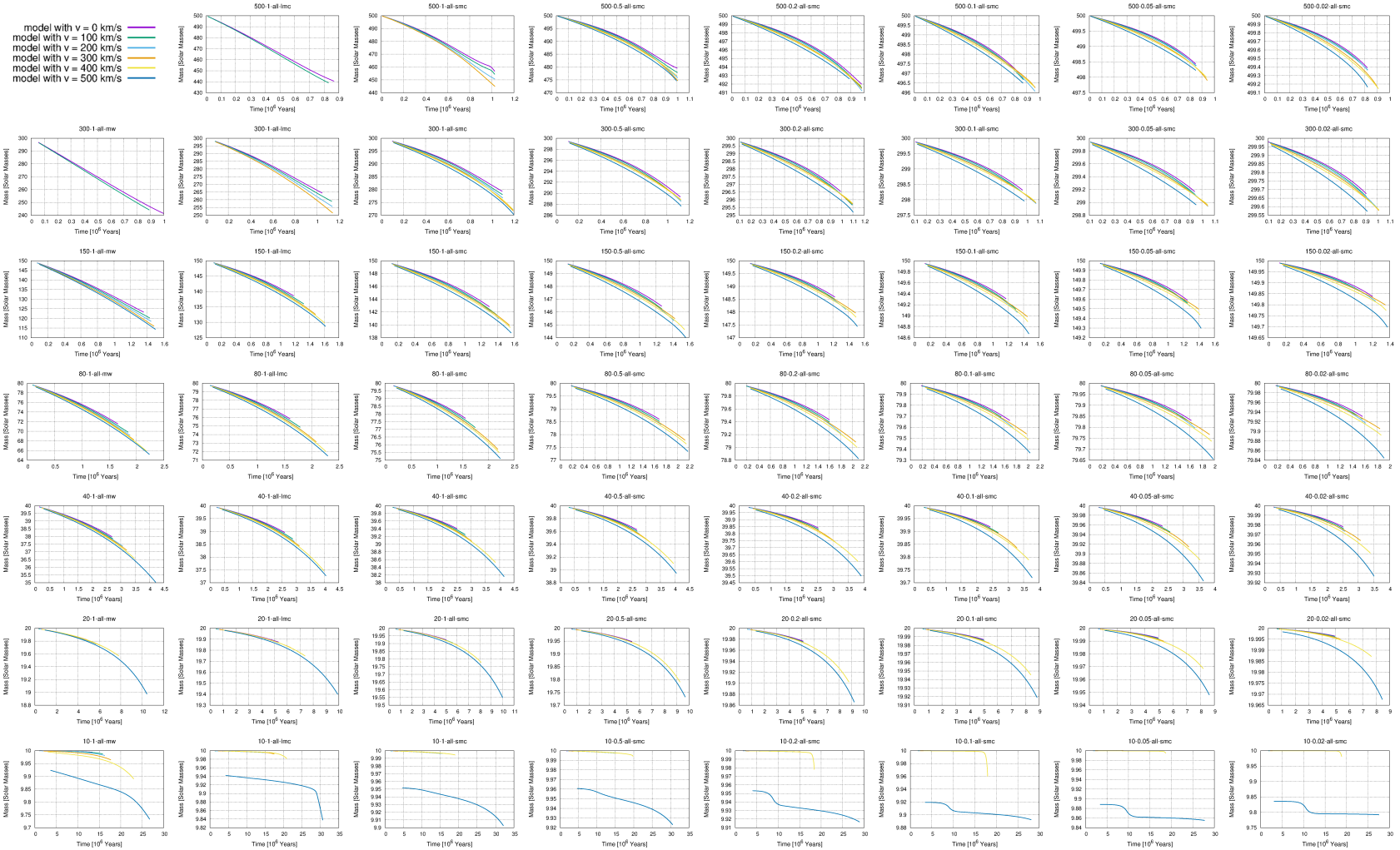

Figure 20: The bulkplot (cf. 3.1.5 and caption of fig. 16) for the mass of the models (in $M_\odot$) over time (in $10^6\,yrs$) with a flexible mass and time scale. This bulkplot differs from figure 18 in the flexible time scale, facilitating the comparison of lines for multiple initial rotational velocities. Higher velocities lead to a higher massloss, which is explained by the increased mixing of the material, leading to higher opacity in the surface and therefore a higher temperature. In the bottom row the $v_{ini} = 500\,km/s$ lines show atypical behaviour, which is because they cross the keplerian critical rotational velocity. Once those models lost mass and therefore spun down enough to cross this limit again the evolution turns into a similar one to that of the other models.

created with a flexible mass-scale, to facilitate differentiation between the different velocity lines.
The models have increased massloss for higher velocity, which is indicated by the lower lines in the plot. This is due to the higher velocity and resulting increased mixing the elements on the surface are heavier on average. The consequence is a higher opacity (because of their higher cross section regarding momentum transfer) and therefore a higher temperature, which increases the massloss (cf. eq. 20).
Another interesting point in figure 20 is the case of the models with $M_{ini} = 10\,M_{\odot}$ and $v_{ini} = 500\,km/s$.
These models cross the keplerian critical rotational velocity (cf. Gagnier, D. et al. 2019), so that the stars are too fast rotating to stay completely intact (only high rotational velocity close to that critical breakup velocity can facilitate this, as otherwise the effect of rotation by itself is too small. Mind that the increased massloss due to rotation is not because of centrifugal forces in a primary way but instead due to the mixing of the material resulting from the rotation). This results in two effects:
First the model sequence starts its evolution with a lower mass than its lower velocity counterparts. This is because even in the initiation phase the model already loses mass due to rotation, so that once the model sequence reaches the main sequence and starts its hydrostatically stable evolution, its mass is already below the initially set mass of $M_{ini} = 10\,M_{\odot}$.
Secondly there are steep declines in the mass for a few models. This is also an effect of the critical rotational velocity. Since the primary influence of rotation on the massloss can not be disregarded for those high velocities, mass is artificially transferred away from the model to account for that effect. The massloss of those models tends to flatten again once enough mass was lost to become stable. This is because by losing mass the model also loses angular momentum and in the course slows down below the critical velocity.

This phenomenon can also be seen in a graph of massloss vs. time (cf. fig. 21). Here one can see that for the mentioned parameter sets ($M_{ini} = 10\,M_{\odot}$ and $v_{ini} = 500\,km/s$) there is hat-like behaviour in the graphs, which indicates the increased massloss for that period of time. After reaching a low enough mass the massloss drops and the line in the graph starts to follow a tendency similar to the rest of the models due to the spin-down.

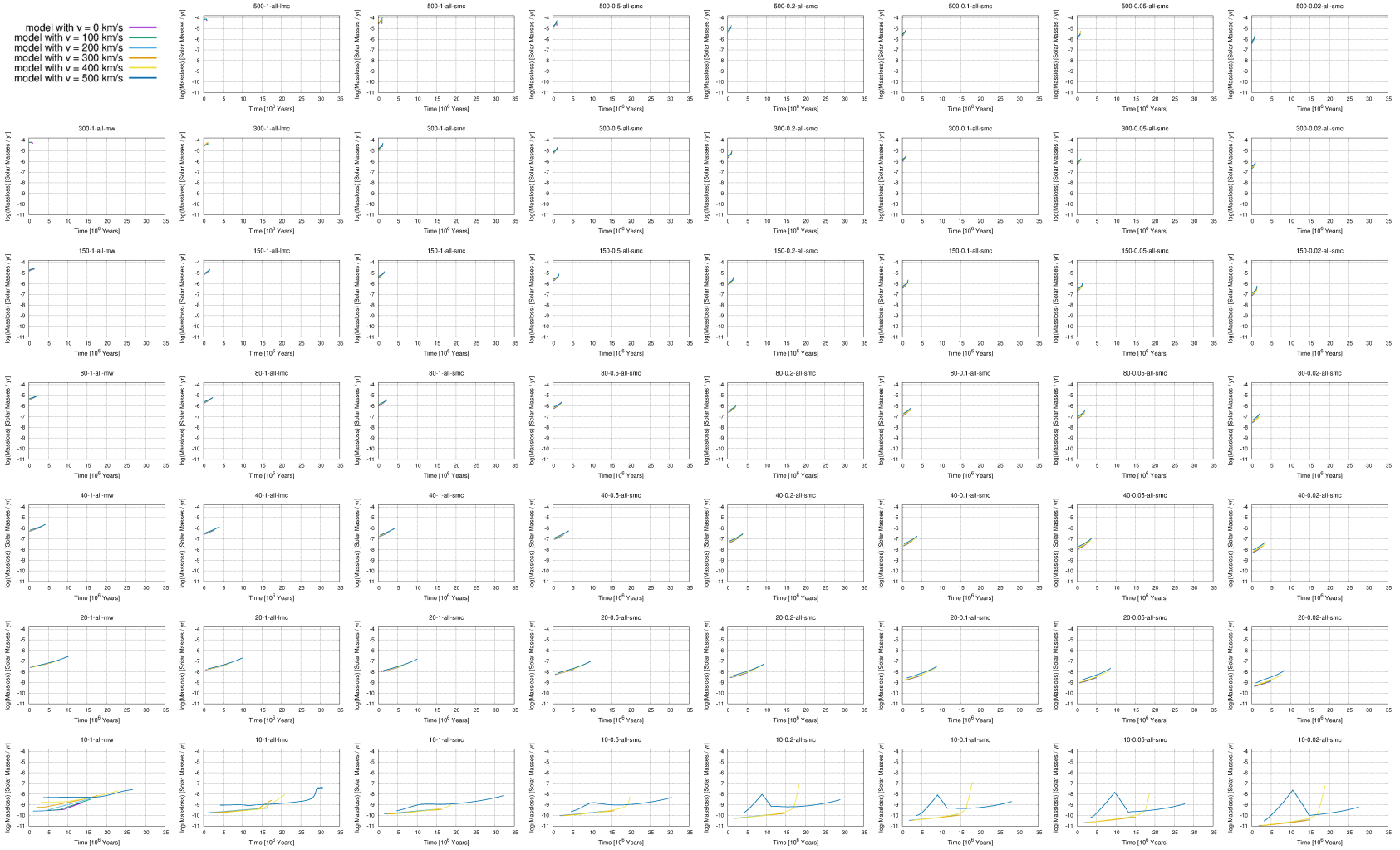

Figure 21: The bulkplot (cf. 3.1.5 and caption of fig. 16) for the massloss of the models (in $M_\odot$) over time (in $10^6\,yrs$) with a fixed linear scale. Striking are the model sequences with $M_{ini} = 10\,M_\odot$ and $v_{ini} = 500\,km/s$, where a hat-like behaviour is displayed. This is due to the increased massloss for those models resulting from the initial rotational velocity being beyond the critical breakup velocity (cf. fig. 20). After losing mass and angular momentum the evolution changes, adopting a trend similar to those close to it in the initial parameter space.

4.3 Hertzsprung-Russell Diagram

In figure 22 a bulkplot of the HRD (cf. 3.1.1) is depicted. The diagram is plotted with dots for equal time steps (isochrone dots, representing $(10^5\,yrs)$). Also in figure 23 an exemplary cutout is given for better accessibility.
The isochrone dots indicate a differing evolution length, which is supported for example by the Y_C diagram (cf. 16). Less massive stars tend to have a longer lifetime with much more dots in their evolutionary paths than the more massive ones.
Interesting in this graph is the bifurcation of the paths; there are those that develop from the middle towards lower temperatures (to the right) and those that develop towards higher temperatures (to the left).
On the one hand there is a certain type of model that cools down in its evolution and therefore expands (explained due to the Stefan-Boltzmann law $L = 4\pi r^2 \sigma T^4$) into red supergiants.

On the other hand one can find some blueward evolving model sequences on the left side of some graphs. This blueward evolution is indicator of CHE as described in section (2.1.4 in the paragraph about differing evolutionary pathways). This kind of evolution can lead to so-called Transparent Wind Ultraviolet Intense Stars (TWUIN stars, cf. Szécsi et al. 2015), which have an optically thin wind and emit intense ionizing radiation.
Apart from NE, which can in the extremely cool (right) case reach stages of the red supergiants, and CHE, found on the left side of the HRD, there are also models that are populating some in-between region, the models undergoing transitionary evolution. These stars either start of their evolutionary paths moving leftwards and then due to spin down change to NE, or start normally evolving and lose their outer shells to uncover helium-rich layers beneath, which also shows strong ionising wind and higher helium abundances on the surface. This can be seen for example in figure 23 for the $M_{ini} = 80\,M_\odot$, $Z_{ini} = Z_{LMC}$, $v_{ini} = 300\,km/s$ model. In figure 22 one can see such a behaviour for example for the high velocities in the $M_{ini} = 10\,M_\odot$ regime, where the lines in the graphs are first moving leftwards to then make a turn and continue their evolution towards cooler regions.
One can also see dependencies on the free parameters: CHE is definitely favoured for lower initial metallicities and higher initial velocities (as for example seen at the $v = 300$ and $400\,km/s$ line for $M_{ini} = 150$ and $300\,M_\odot$ in fig. 23). The mass-dependency is harder to identify, as the models do not reach the end of the main sequence yet, which means that it is more difficult to discern between CHE and TE (as seen in the $M_{ini} = 10\,M_\odot$ regime). Nonetheless the graphs seem to follow the general rule that higher masses are also favourable for CHE. This can

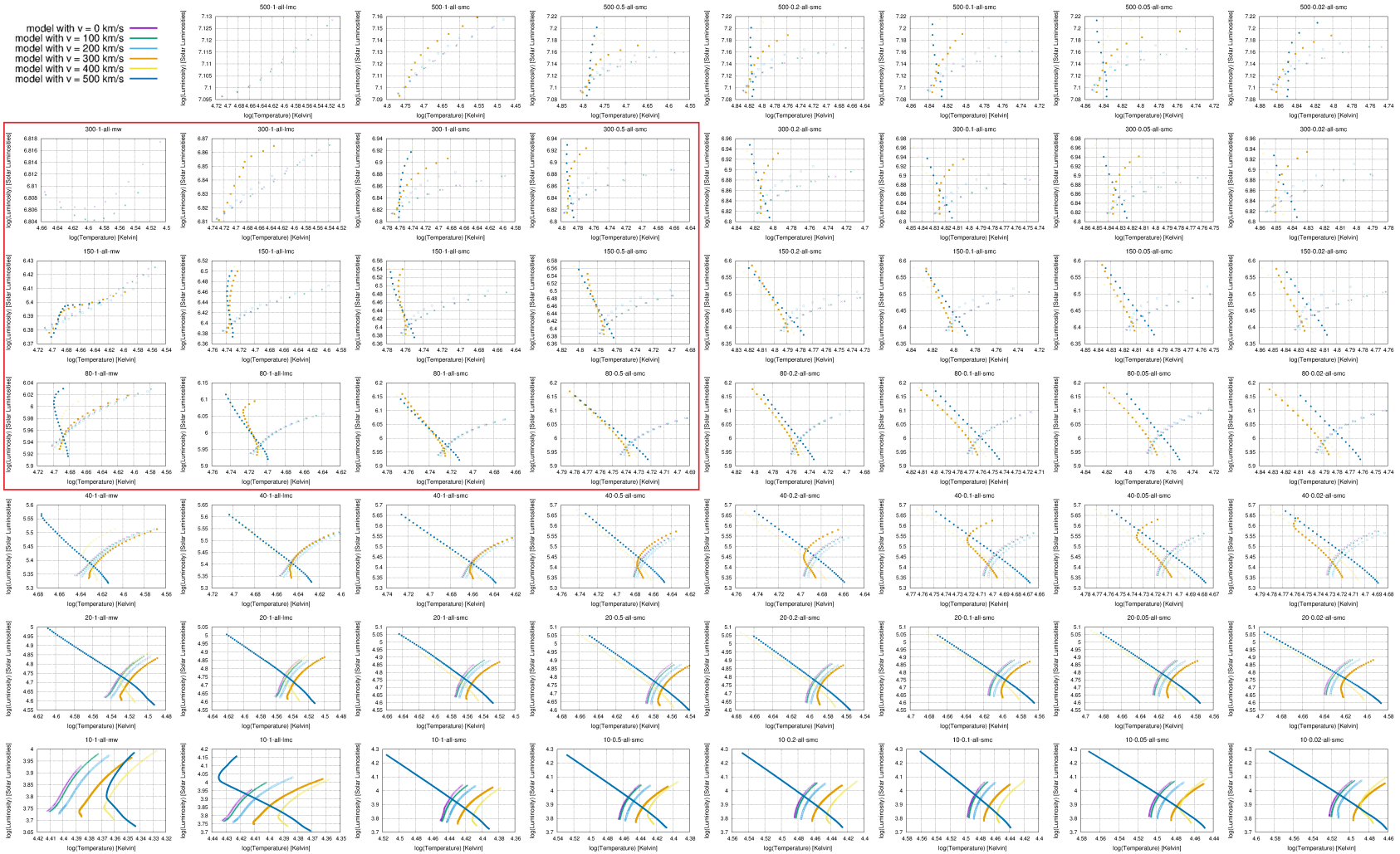

Figure 22: The bulkplot (cf. 3.1.5 and caption of fig. 16) for the Hertzsprung-Russell diagram (HRD, cf. 3.1.1) of the model sequences, displayed with isochrone dots in $10^5\,yrs$ steps. In the HRD the luminosity (in $L_\odot$ with a logarithmic scale) is plotted vs. the temperature (in K, with an inverted logarithmic scale). The red rectangle indicates the area that is displayed again zoomed-in in figure 23. It is shown that there are two main ways the sequences can evolve, either moving rightwards into cooler temperatures, indicating a normal evolution (cf. 2.1.5), or moving leftwards into hotter temperatures, indicating chemically homogeneous evolution. There are also some models showing signs of transitional evolution, indicated by lines that turn around from a leftward into a rightward evolution. There is a preference of the homogeneous evolution for lower initial metallicities and higher initial velocities. For high initial masses the tendency of transitional evolution increases, broadening the area of initial velocity that leads to TE. Due to the amount of isochrone dots it is also shown that the sequences with low mass have a longer lifetime than the more massive ones.

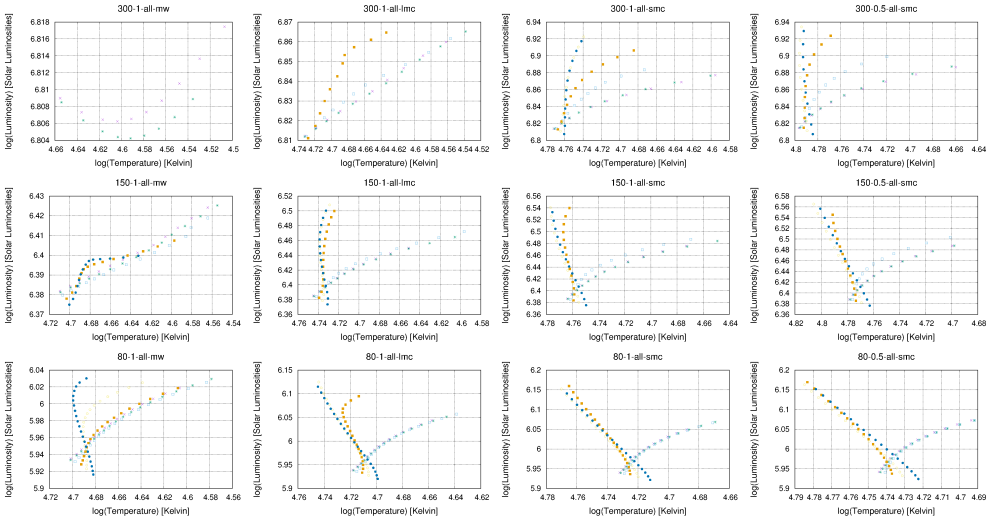

Figure 23: Exemplary cutout of the bulkplot (cf. 3.1.5 and caption of fig. 16) for the HRD (cf. 3.1.1) of the models, fixed on $M_{ini} = 300$ to $80\,M_{\odot}$ and $Z_{ini} = Z_{MW}$ to $0.5{\cdot}Z_{SMC}$. This cutout highlights the dependency of the evolutionary pathways (cf. 2.1.5) on the initial parameters. Chemically homogeneous evolution (leftward evolution towards hotter temperatures) favours low-metallicity and high initial velocities.

for example be seen in the comparison of the $400\,km/s$ line for low metallicities. There seems to exist a caveat however: At some point CHE seems to become less likely again, as the line starts to turn towards the right hand side again for the models with mass $M_{ini} \approx 150\,M_{\odot}$. This is not surprising, considering that TE becomes more likely for higher masses (as can be seen in fig. 14 and Szécsi et al. (2015) in the broadening of the yellow region for high masses, and also in 4.4).

4.4 Surface Helium Mass Fraction

In figure 24 one can see the Surface Helium Mass Fraction vs. Time.
As the homogeneously evolving models contain a homogeneous mix of all the material, the whole amount of abundant hydrogen gets burned during the main sequence. This means that the helium mass fraction on the surface rises just as it does in the core. This is in contrast to the NE models, where the fusion processes only happen in the core, which leaves the envelope about untouched.
This is mirrored in figure 24. There are some models, where the Helium Mass Fraction at the surface stays the same throughout the whole lifetime, whereas others' rises up till the point of around 60%, which is because the models only run up to the point of $Y_C = 0.6$, which in the case of CHE also means $Y_S \approx 0.6$.

Additionally the models undergoing TE are shown with graphs where the end-point of the evolution is between $Y_C = 0.6$ and 0.24, which is due to either

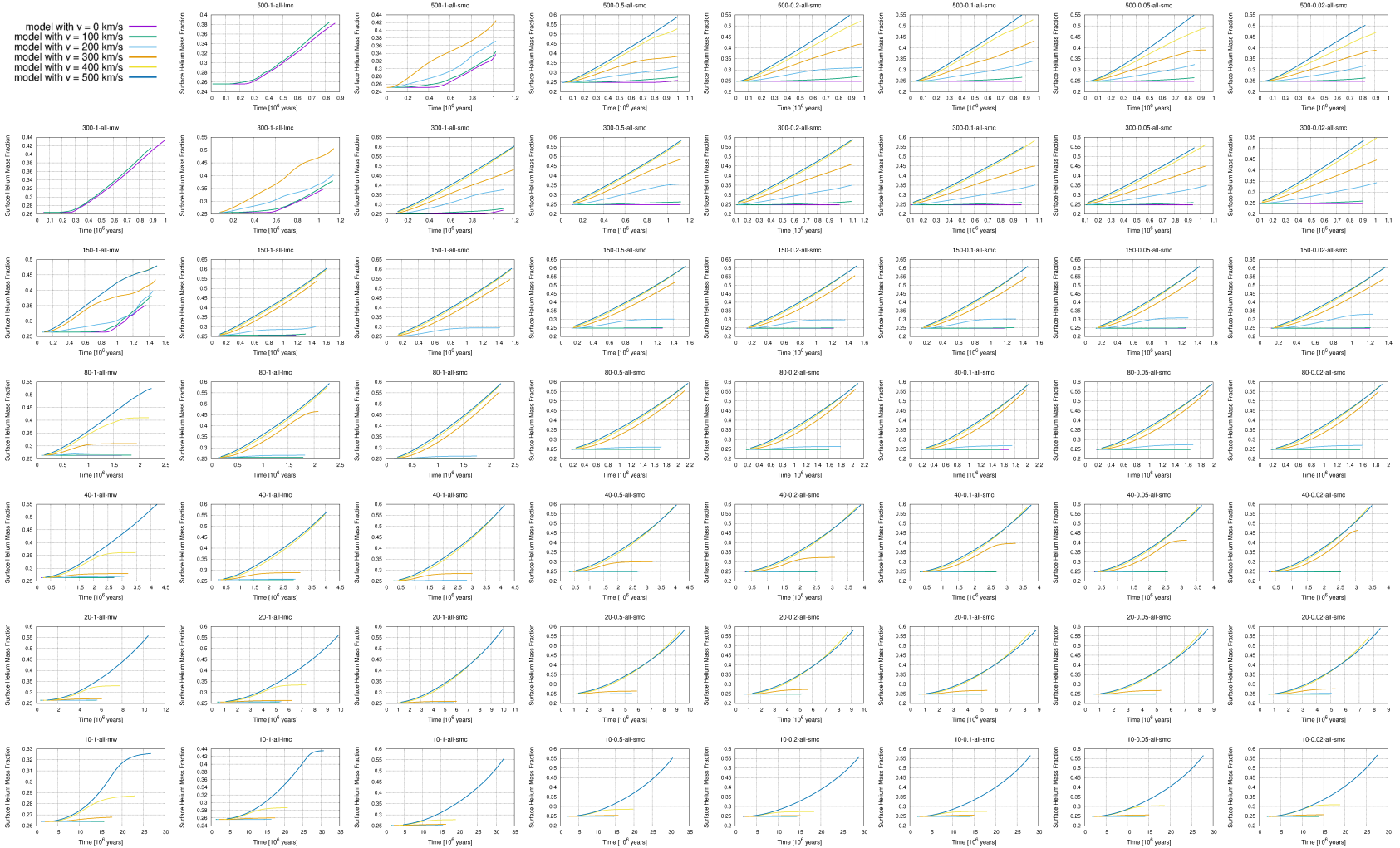

Figure 24: The bulkplot (cf. 3.1.5 and caption of fig. 16) for the surface helium mass fraction of the models over time (in $10^6\,yrs$). There are sequences depicted steadily increasing their surface helium abundance, up to the end point of around 60%, showing that the abundance at core (at the end $Y_C = 0.6$) and surface are about the same, indicating a chemically homogeneous evolution (cf. 2.1.5). On the other hand there are sequences shown that keep the surface helium abundance constant through the lifetime, indicating an untouched surface and therefore a normal evolution. There are also some models reaching intermediate helium abundances on the surface, which can result from transitional evolution, either starting chemically homogeneously evolving and then changing to NE due to spin-down, or normally evolving but shedding outer layers due to high rotation and uncovering helium-rich layers beneath.

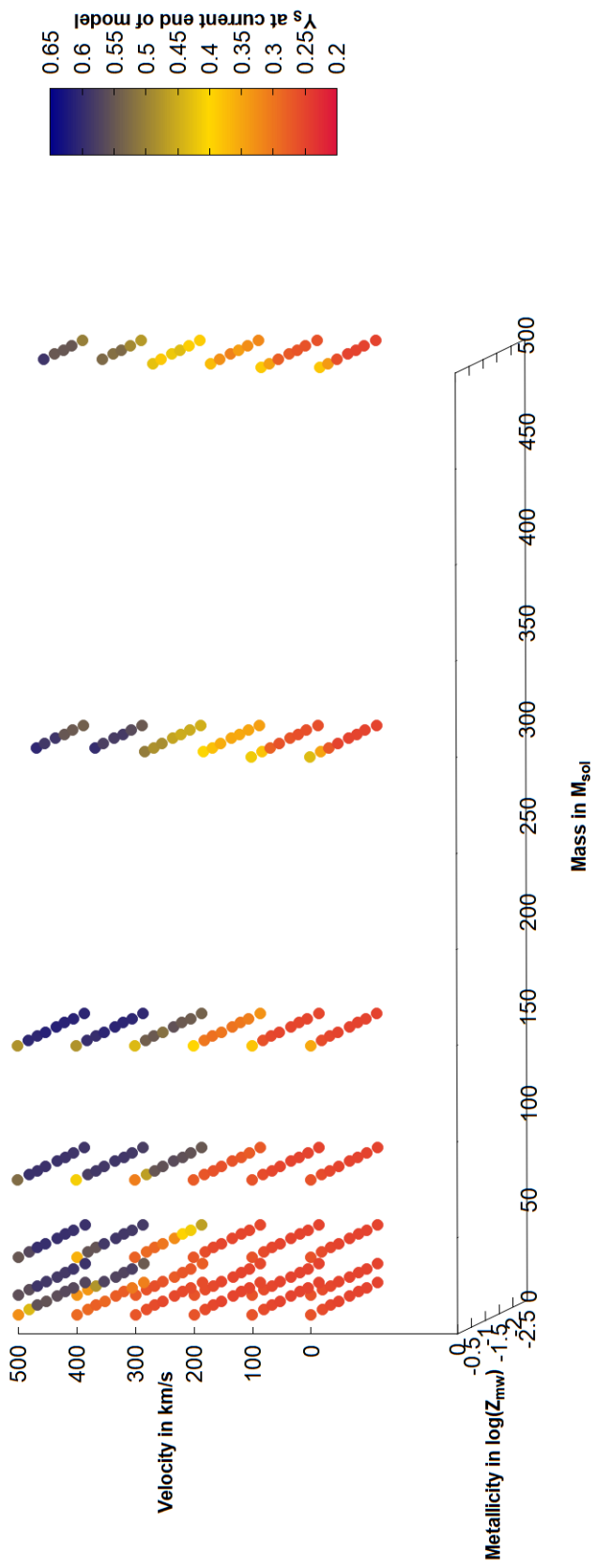

Figure 25: Plot of the Surface Helium Mass Fraction for the whole parameter space (initial mass in $M_\odot$, initial rotational velocity in km/s, initial metallicity in $\log(Z_{MW})$) as a colour plot (cf. 3.1.4). Each dot indicates one evolutionary model sequence at the end of its current lifetime, coloured according to the surface helium mass fraction at that time. Red more or less corresponds to a normal evolution, blue to a chemically homogeneous one. Yellow can indicate a transitional evolution, although it has to be stressed that the distinction between TE and CHE is not clear since the sequences did not finish the main sequence yet. This figure (in contrast to fig. 26 and fig. 31) is showing the plot about head-on the mass-velocity plane. Here one can see the broadening of the yellow area (indicating TE) for higher initial masses regarding the initial velocity.

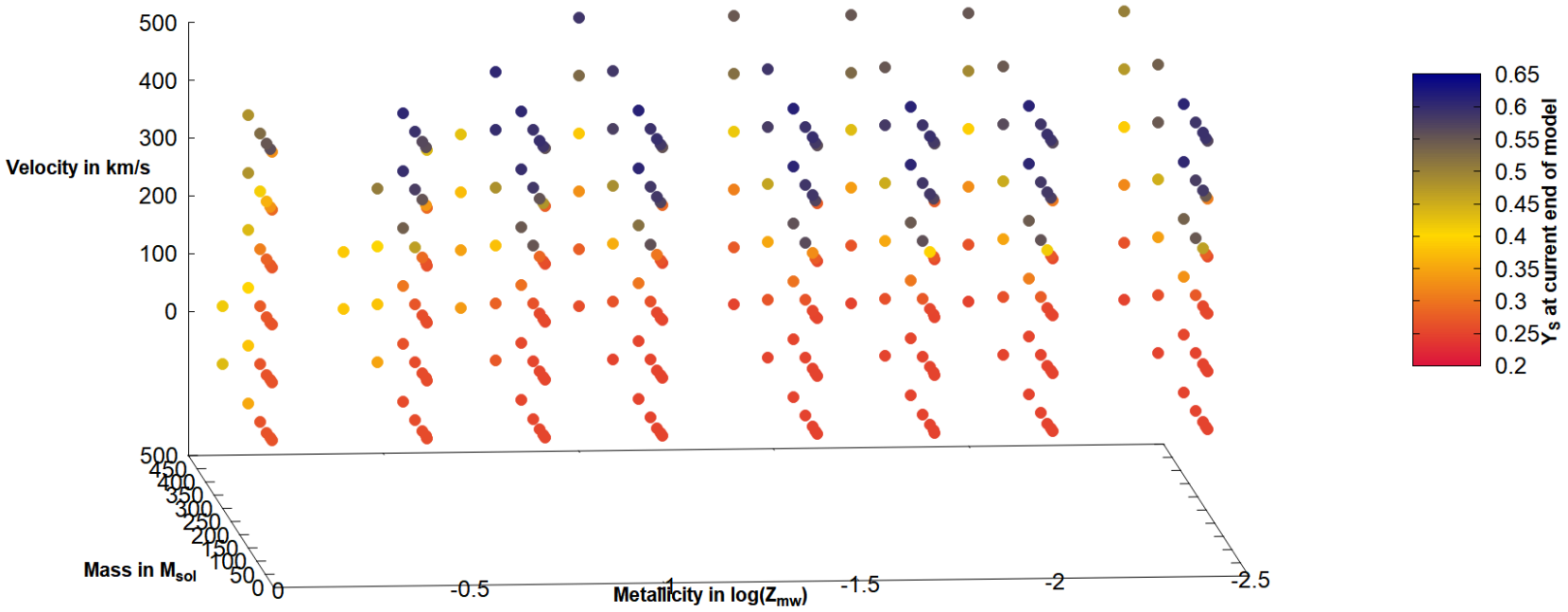

Figure 26: Plot of the Surface Helium Mass Fraction for the whole parameter space as a colour plot (cf. 3.1.4 and the caption of fig. 25). This figure (in contrast to fig. 25 and fig. 31) is showing the plot from the perspective of the metallicity-velocity plane. Here it is shown that CHE is preferred for low initial metallicities, as the limit of the initial velocity is decline with decreasing initial metallicity.

spin-down of former chemically evolving models or the uncovering of helium-rich layers due to massloss (cf. 2.1.5). Examples of this behaviour are the models with intermediate initial rotational velocity, high mass (for example $M_{ini} = 500\,M_{\odot}$) and low metallicity ($Z_{ini} = 0.5\,Z_{SMC}$ to $0.02\,Z_{SMC}$).
To distinguish between TE and CHE for a given model one would have to continue the computations of the evolutionary sequences to the end of the main sequence, as the difference between both kinds can be hard to see when the models are stopped short, since it is not determined whether the model sequence will spin down enough to change their evolutionary path. Nevertheless one can see the same tendency as in Szécsi et al. (2015): Low values of surface helium mass fraction at the end of the sequence for slow rotators, indicating NE, high values (up to the maximum value and same composition as $Y_C = 0.6$) for fast rotators with a blueward evolution in the HRD, and intermediate values for TE.
To get an overview of the evolutionary models and their different pathways one can also look at the (current) end state of the evolution; in figure 25 and figure 26 one can see the last point of evolution the models reached, depicted in the 3D parameter space and with a colour coding indicating the amount of helium at the surface (cf. 3.1.4).
To improve the accessibility of the graph here also two different perspectives are provided, with a third in the appendix A.1 in figure 31.
There is a distinction between different kinds of model sequences here as well, with areas of high surface helium mass fraction (≈ 0.6, blue dots), areas of low one (≈ 0.3, red dots) and areas of intermediate one (yellow dots).
Comparably to figure 14 there is a trend of CHE for fast rotators and one for NE for slow rotators. Also the broadening of the yellow area similar to figure 14 for high initial masses is visible in figure 25.
CHE is also preferred for low initial metallicities, as can be seen in figure 26, as the velocity-limit to facilitate CHE decreases with decreasing initial metallicity.

4.5 Abundance Plots

In figures 27 - 29 one can see exemplary diagrams of the abundance vs. the mass coordinate (cf. 2.2.1). The examples were chosen to highlight the differences in CHE, TE and NE.
Figure 27 shows graphs for $M_{ini} = 10\,M_{\odot}$, $Z_{ini} = Z_{MW}$ and no initial rotational velocity. The top panel is from the beginning, the middle from the middle and the bottom from the end of the evolution (as indicated by the legend for the time t).
At $M \approx 4\,M_{\odot}$ the line for the helium fraction (blue line) and the one for the

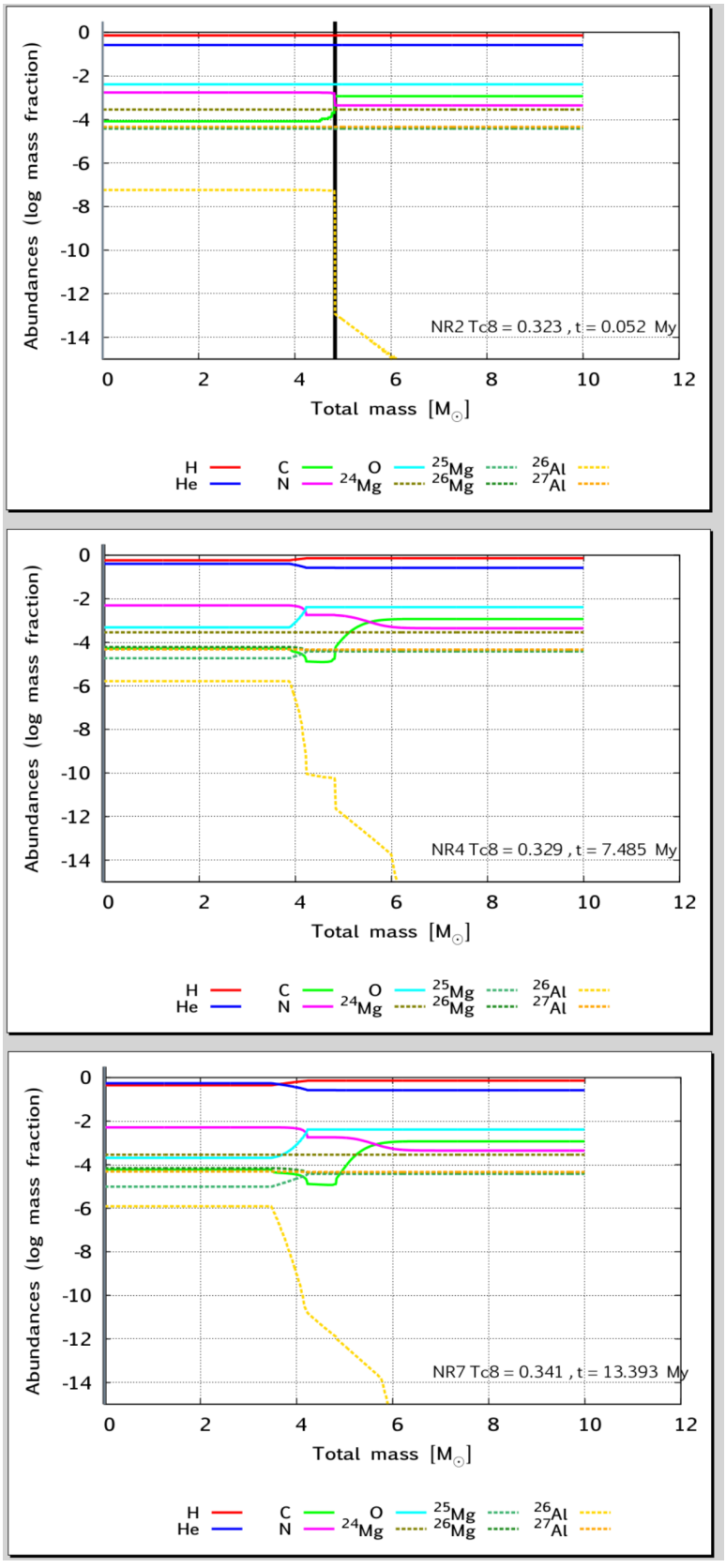

Figure 27: The composition plots (cf. 3.1.3) of a $M_{ini} = 10\,M_{\odot}$, $Z_{ini} = Z_{MW}$ model with no initial rotational velocity against the mass coordinate in arbitrary time steps. The first panel shows the graphs of a time point in the beginning of the evolution, the middle panel an intermediate point and the bottom panel a point at the end. The logarithmic abundance of various elements and isotopes (H, He, C, N, O, ^{24}Mg, ^{25}Mg, ^{26}Mg, ^{26}Al, ^{27}Al) is plotted in different colour lines against the mass coordinate (cf. 2.2.1) in units of $M_{\odot}$. This is an example of a model sequence undergoing normal evolution: The border between core and envelope is shown as the mass where hydrogen and helium abundances exchange their dominance over time (red and dark blue lines cross at around $4\,M_{\odot}$), as in the core the hydrogen is converted into helium, whereas the envelope does not take part in fusion processes and therefore keeps the initial abundance ratios. Additionally one can see that the MgAl-Cycle (cf. 2.1.3) is influencing the abundance of Mg and Al in the core, which results in differences compared to the abundances in the envelope.

hydrogen fraction (red line) cross (which can be seen in the middle and bottom panel). Below that crossing point the fusion processes affect the abundance, therefore changing for example the helium fraction over time, whereas above that mass there is no change through the whole evolution. This is an example of a model sequence following a normal evolutionary path.
The crossing point is especially easy to spot as the ^{26}Al abundance drops at that point. This is because ^{26}Al is steadily produced in the core as part of the MgAl-Cycle (cf. Langer 2012a and 2.1.3), so that its abundance stays about constant there. Outside of the core however the abundance drops over time as it is undergoing β^+ decay or electron capture (cf. Basumina & Hurst 2016).

In contrast to figure 27 one can see graphs for different time points of the model sequence for $M_{ini} = 300\,M_\odot$, $Z_{ini} = Z_{SMC}$ and $v_{ini} = 500\,km/s$ in figure 28. Here is no crossing point, because all the material in the homogeneous mass of the model is used as fusion material, which results in the change of the constitution up till the very edge of the star. There is effectively no strict core and envelope structure any more. This is an example of a model homogeneously evolving.

In figure 29 the graphs for three time points of the model sequence with $M_{ini} = 300\,M_\odot$, $Z_{ini} = 0.02\,Z_{SMC}$ and no initial rotational velocity are depicted. There is a crossing point visible at $M \approx 250\,M_\odot$, but in contrast to the plots of the NE it is closer to the surface, indicating almost but not quite complete mixing of the star's material. This is an example of a model sequence undergoing transitional evolution.

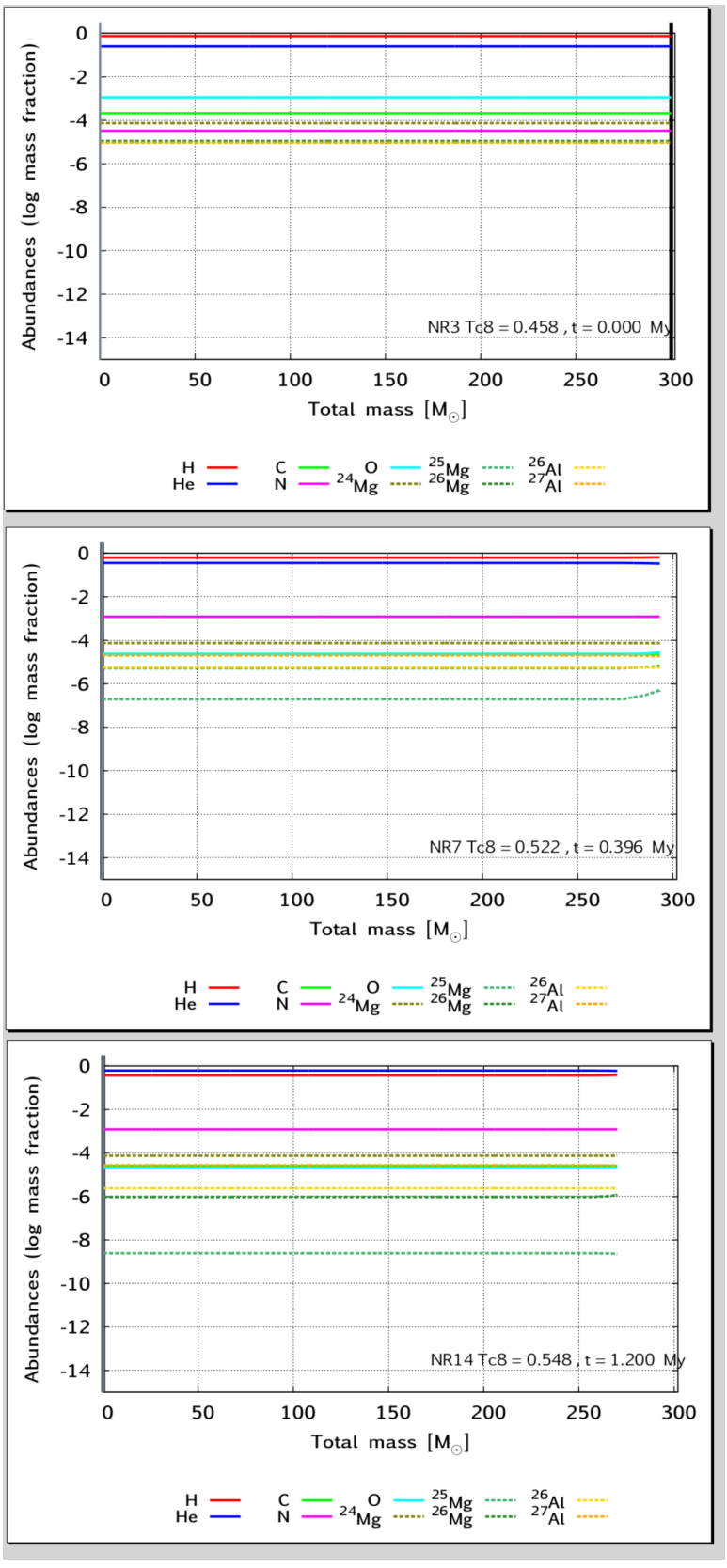

Figure 28: The composition plots (cf. 3.1.3 and the caption of fig. 27) of a $M_{ini} = 300\,M_{\odot}$, $Z_{ini} = Z_{SMC}$ and $v_{ini} = 500\,km/s$ model sequence against the mass coordinate in arbitrary time steps. This is an example of a chemically homogeneous evolution: In contrast to figure 27 one cannot see a crossing point between core and envelope due to the homogeneous distribution in the model. The abundances are the same throughout the complete star.

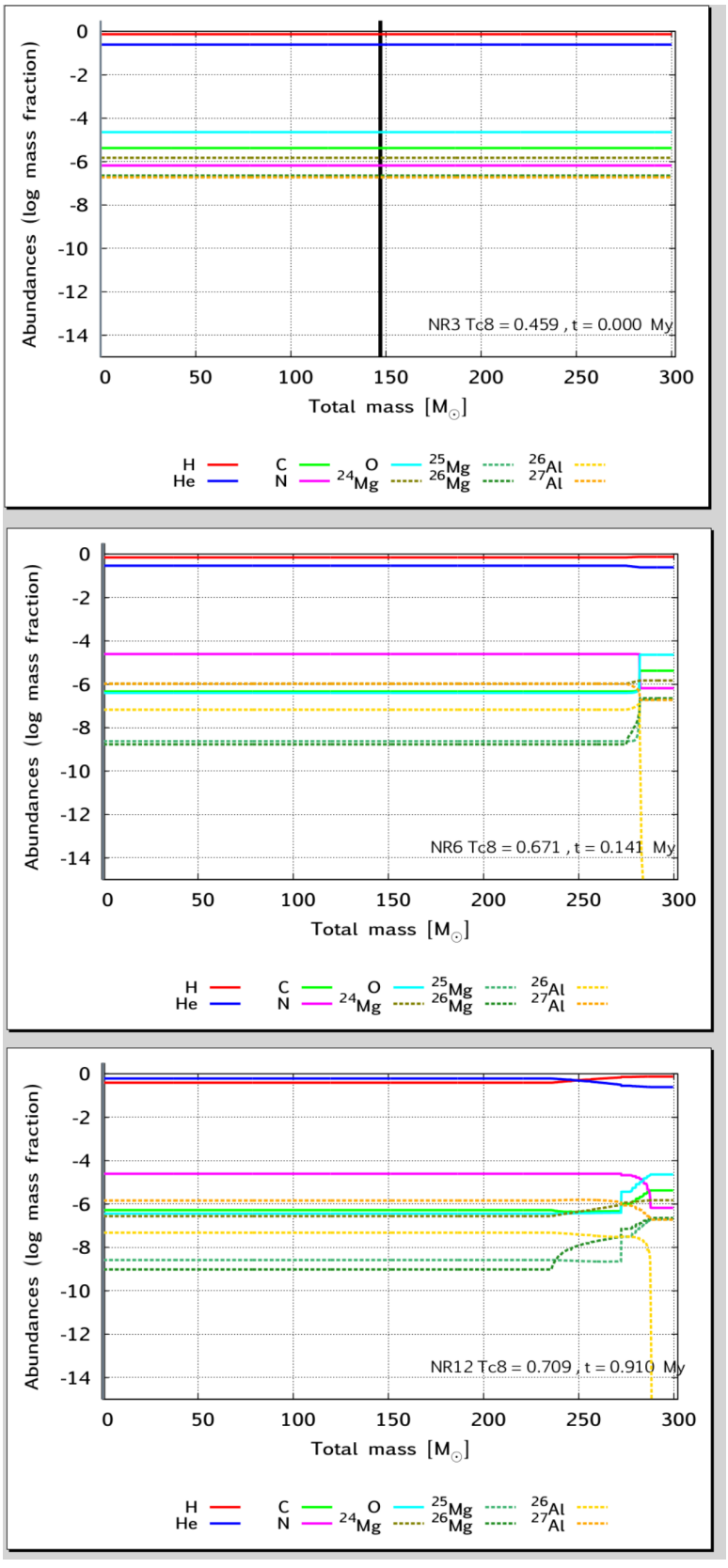

Figure 29: The composition plots (cf. 3.1.3 and the caption of fig. 27) of a $M_{ini} = 300\,M_{\odot}$, $Z_{ini} = 0.02\,Z_{SMC}$ model with no initial rotational velocity against the mass coordinate in arbitrary time steps. This is an example of a plot for a Transitional Evolution: Similar to figure 27 one can see a crossing point between core and envelope, but unlike in NE the crossing point is at a much higher mass compared to the complete mass of the model ($\sim 275\,M_{\odot}$ of $300\,M_{\odot}$). The star has therefore a bigger envelope, which is due to the mixing in the star. Not quite the whole mass of the model is mixed into a homogeneous mass, but the influence of the fusion reaches further than in a normally evolving model.

5 Discussion

The models created provide a broad grid to support other works on. Here some advantages will be listed for future usage:

5.1 The Models Close to the Eddington Limit

As can be seen in the bulkplots some models do not reach the set target of $Y_C \approx 0.6$. This is due to their closeness to the Eddington limit, which prevents their physical evolution. This applies strictly to all velocities of the M=500 $M_\odot$ and Z=Z_{MW} and also some velocities for the neighbouring parameter sets (M=500 $M_\odot$, Z=$Z_{LMC/SMC}$ and M=300 $M_\odot$, Z=$Z_{MW/LMC}$).
Even though those models did not complete, it is still a result matching the expectations, because in reality stars with that high masses are indeed not observed at those metallicities. Other models also predict some kind of upper limit to the mass of stars (like for example Vink, Jorick S. (2018)) and also propose it to be metallicity-dependent, so the findings at hand are in accordance with other literature.

5.2 Basis for SILCC Simulations

As introduced before in 1.1 the aim of the SILCC project (cf. Walch et al. 2015) is to simulate the evolution of the interstellar medium and the life cycles of molecular clouds. For the stellar feedback to be accurate, models of the stars need to be accessible to populate the simulation with them.
The thesis at hand provides such models for a wide range. In contrast to works like Gatto et al. (2016), where models with solar metallicity from Ekström et al. (2012) were used, and Brugaletta (2021) with used models having four metallicities from Szécsi et al. (2022), the present work provides a whole range of metallicity models from $Z_{ini} = Z_{MW}$ down to $Z_{ini} = 0.02\, Z_{SMC}$. This can be useful since, as seen in 4, the models sometimes vary quite drastically, a good example of that being the CHE, which does not happen in a high-metallicity environment. Since the stars undergoing CHE have a completely different kind of massloss, based on that of a Wolf Rayet star, than stars with NE, such a grid of models can give a tool in estimating the effect of metallicity of the stellar models on the evolution of molecular clouds.
The biggest caveat in this regard is the run length of the present models. In contrast to the models from Ekström et al. (2012) and Szécsi et al. (2022) only runs up to 0.6 of the main sequence were created (for now), which falls short of the other two works. Therefore a continuation of the present models would be

beneficial to get to the same validity for those latter part of the evolution.

5.3 Chemically Homogeneous Evolution

As one can see from the graphs in 4, the free parameters of initial mass, initial rotational velocity and initial metallicity all have impact on the development of the stars. The pathways for example in the HRD differ depending on all three, giving way to CHE, TE and NE in the following way:
Lower initial metallicities favour the phenomenon of CHE. This is understandable, as lower metallicities mean there are fewer heavy ions in the atmosphere of the star, resulting in a smaller cross section with the radiation (cf. Fornalski 2018 eq. 3 and 4) and therefore a lower massloss and loss of rotational velocity. Keeping up a high velocity ensures a more impactful mixing due to centrifugal forces, which enables the formation of homogeneously evolving stars.
Higher initial velocities therefore also increase the probability for the emergence of CHE, as the model starts in a faster rotating state. If it manages to not spin down too much (due to decreased massloss or efficient angular momentum transport from inside to the outside) this also can result in CHE.
Higher initial mass seems to favour this behaviour as well, although that is harder to discern in the graphs than the other two dependencies.
One also has to stress that these models could be able to give more information regarding this specific aspect of evolutionary differences once they are continued at least until the end of hydrogen burning, as one then would be able to tell apart CHE and TE more easily. This means that a further continuation can be beneficial for more investigation in that regard.

5.4 Massloss

There are some clear differences for the various parameter configurations seen in figure 20 and figure 21. They were to be expected based on the massloss formulas from Vink et al. (2000) and Vink et al. (2001), but having models using those parameters over a wide range of initial metallicities can still help confirm and improve on the validity of them. By continuing the models one can see whether the assumptions of massloss apply to them by checking for abnormalities and unpredicted behaviour. If those appear, it is a sign for the need to modify it (depending on the circumstances of the abnormalities), if they do not, it can be a confirmation of the massloss formula used.
As said before in general the graphs for mass and massloss look as expected, with only few exceptions being conspicuous. One of the main areas is that of $M_{ini} = 10\,M_{\odot}$ and $v_{ini} = 500\,km/s$, which has increased massloss and shows

some abnormal shape in all the graphs. It is explained by the fact that these models are beyond the critical rotational velocity (cf. Gagnier, D. et al. 2019) and therefore lose a lot of mass in short time. Nevertheless it is a striking feature that could be investigated more to confirm that claim; if it is a physical phenomenon that could be observed in the real world, actual observations of it would be ideal. A star losing so much mass could for example have a decretion disk that could then be studied (cf. Krtička et al. 2011).
If on the other hand it is not physical, that would imply some limit to the parameters; It would follow that below a certain mass or above a certain velocity stars could not exist like it is predicted in the model. If that was the case it should be investigated why that is and in how far those limits apply in reality.
Additionally the models can be used to investigate the massloss in a more detailed manner, for example by means of spectral analysis (cf. Kubátová et al. 2019). In the mentioned work three homogeneously evolving models (with M_{ini} = 20, 59 and 131 $M_{\odot}$) were used at varying points of their evolution (minding two possibilities of massloss and two of wind clumping) to determine their expected spectra by using the Potsdam Wolf-Rayet (PoWR) stellar atmosphere code. As the thesis at hand provides a wide range of models, some of which being stars who display signs of CHE, the same could be done for those models, giving way to a much broader investigation.

5.5 TWUIN Stars and Long Duration Gamma Ray Bursts

After stars end their regular lifetime of fusion processes, there are multiple ways for them to end in. For massive stars specifically there are very disrupting events like for example supernovae (SNe), superluminous supernovae (SLSNe) and γ-ray bursts (GRBs) (cf. Garcia et al. 2021, Quimby et al. 2013, Soderberg et al. 2006). There is a preference of long duration GRBs and SLSNe observed in metal-poor galaxies (cf. Leloudas et al. 2015) that makes models like the one at hand useful for investigations on the effect of metallicity on these events.
TWUIN stars like the ones mentioned in section 4.3 are possible progenitors for long duration GRBs: In general it is often assumed that long duration GRB ($>$2 s) are produced by the so-called collapsar scenario (cf. Woosley 1993, Piran 2005 in chapter 9). Here the iron core of a massive, fast rotating star is collapsing, creating a black hole with an accretion disk. To account for the angular momentum that needs to be syphoned out of the system when the material of the disk is falling into the black hole two opposing high-energetic beams perpendicular to the disk emerge. Afterwards the energy of the beams gets dissipated internally and creates the GRB. The beams also interact with the surrounding

matter, which creates an afterglow (cf. Piran 2005).
This means that a better investigation of those progenitors could help understanding long duration GRB (and SLSNe), which makes the present work a first step to a deeper research by providing the models needed.

5.6 Gravitational Wave Research

With the arrival of setups like the (advanced) Laser Interferometer Gravitational-Wave Observatory (aLIGO) (cf. Aasi et al. 2015) a whole field of research opened up. Their data is originating from the remnants of binary massive stars (cf. Abbott et al. 2016, Ricci 2019), namely either neutronstar or black hole mergers or a combination of both.
To improve on their research a prediction for such events would be useful. With models for massive stars such as the ones provided for the present work one can attempt to synthesize a population of stars by means of a stellar mass distribution function. Once that is done one then can get projected rates and similar useful things from it to apply it to gravitational wave research.
Additionally short duration GRB ($<2\,\mathrm{s}$) can be investigated in conjunction with gravitational wave research, since they are often companions of the mergers of two massive objects like neutron stars or black holes (cf. Szécsi 2017). With this, the models at hand provide a basis for research of both long- and short-duration GRB.

5.7 Abundances and Globular Cluster Studies

Supergiants can play a big role in the creation of multiple stellar populations in globular clusters that are observed in almost all of them (cf. Szécsi et al. 2018). One theory is that the first population of stars in the young clusters (YCs) can consist of cool supergiants, which are surrounded by a "photoionization-confined shell" (PICO shell) around them (created by the interaction of the stellar wind of the supergiant and the ionisation front of TWUIN stars) and creating the new (and polluted) generation of stars there.
Another theory works without the PICO shell (cf. Szécsi & Wünsch 2019). Here the second generation of stars is born in an area that is created due to the interplay of the stellar winds of cool supergiants and the rapidly cooling environment due to the hydrodynamics of the cluster.
The new stars are fed (polluted) with material from these supergiants, which makes an overview of the abundances interesting for further investigations. Both theories can be investigated further with the new models presented here, as they give a broader data set with varying initial metallicity to work on. By applying

the approaches from the mentioned works one could find constraints to them or strictly reasons to favour one over the other. The two papers mentioned above only used initial models with metallicities of LMC and I Zw 18. Also only models with initial rotational velocities of $v_{ini} = 0$ or $100\,km/s$ were used, which the present work also expands on.
In 4.5 one can see that the models can enable that investigation (although as said before a continuation of the models until a latter time would be advantageous). By comparing the radius and the core-envelope boundary, in addition to the criterion of cool temperature and high luminosity in the HRD, one can differentiate between the Supergiants and models that are not inflated.
One can also see the effects of the MgAl-Cycle in the shown abundance plots by checking the abundances of the magnesium and aluminium isotopes. Inside of the core the abundance stays more or less the same due to the continuous production of ^{26}Al in the cycle, whereas outside of it the abundance of the isotope drops over time due to its radioactive nature.
The effect of the NeNa-Cycle was not investigated yet, that is a possible goal for the future. It falls in line with the other investigations mentioned above.
The lithium abundance investigation is also a goal for the future. This is part of the reason why the model sequences for now end at $Y_C = 0.6$, because the effect of the lithium production and destruction increases going towards the end of the main sequence, so a better resolution of the sequence from that point onward is beneficial for that goal.

5.8 Runlengths and the BoOST Format

The target of around $Y_C = 0.6$ was met with most of the models. This does not necessarily mean that the code will continue to work fine for a further continuation, but one can try and see how many of them actually reach the end of helium burning to give a more complete picture of the evolution. This would also improve the distinction between the TE and CHE models. This could be a future goal for investigations.
The BoOST format can be implemented, although it was left out for this work as it is beneficial to do it for a higher run length, preferably to the end of the helium burning. As can be seen in the present work it is also possible to change the step resolution mid-evolution to increase the sensitivity to changes in critical phases.

A Appendix

A.1 Appendix A

On the following pages additional material is shown for interested readers.

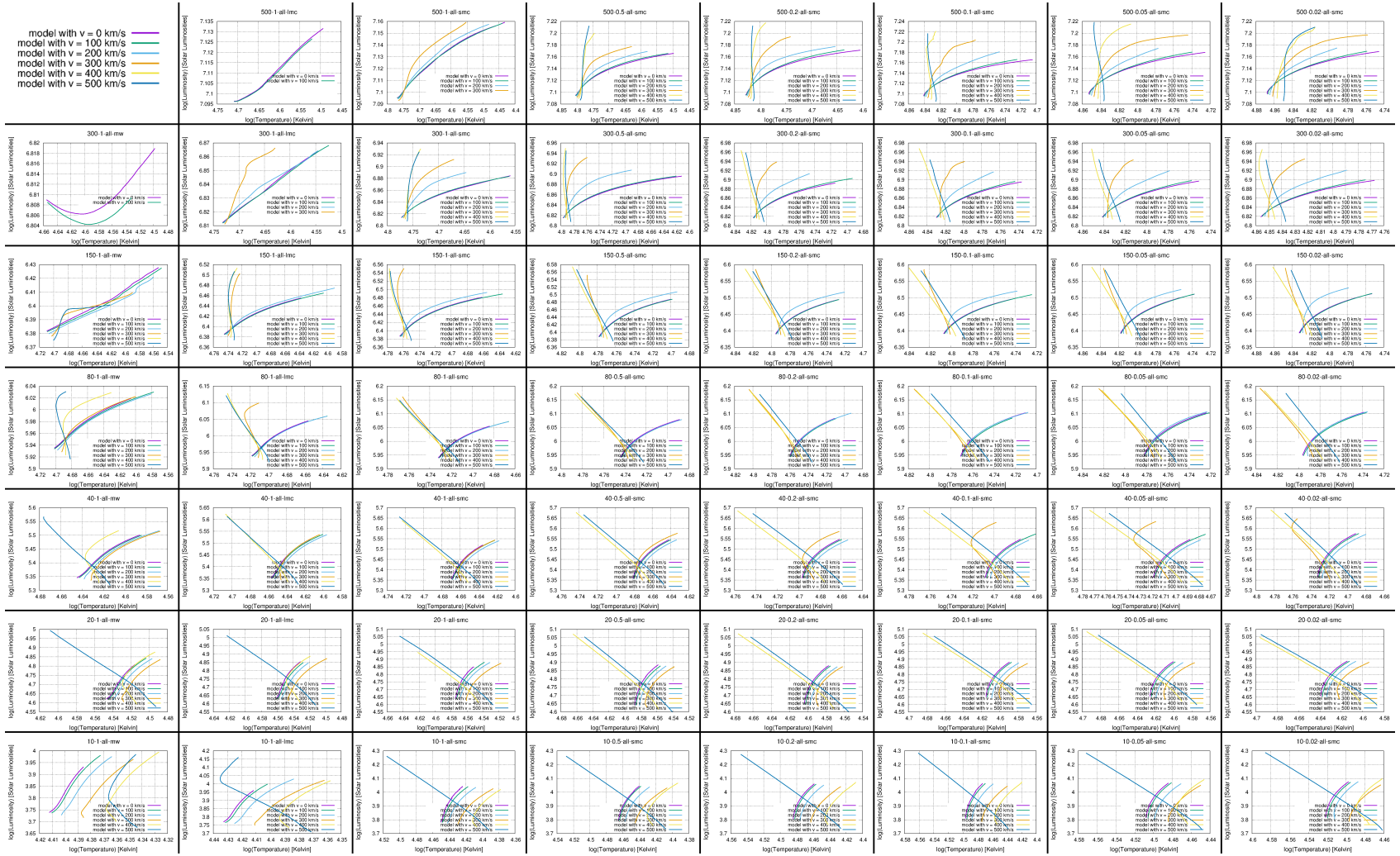

Figure 30: The bulkplot (cf. 3.1.5 and caption of fig. 16) for the Hertzsprung-Russell diagram (HRD, cf. 3.1.1) of the model sequences, without isochrone dots (cf. fig. 22). In the HRD the luminosity (in $L_\odot$ with a logarithmic scale) is plotted vs. the temperature (in K, with an inverted logarithmic scale). It is shown that there are two main ways the sequences can evolve, either moving rightwards into cooler temperatures, indicating a normal evolution (cf. 2.1.5), or moving leftwards into hotter temperatures, indicating chemically homogeneous evolution. There are also some models showing signs of transitional evolution, indicated by lines that turn around from a leftward into a rightward evolution. There is a preference of the homogeneous evolution for lower initial metallicities and higher initial velocities. For high initial masses the tendency of transitional evolution increases, broadening the area of initial rotational velocity that leads to TE. Due to the amount of isochrone dots it is also shown that the sequences with low initial mass have a longer lifetime than the more massive ones.

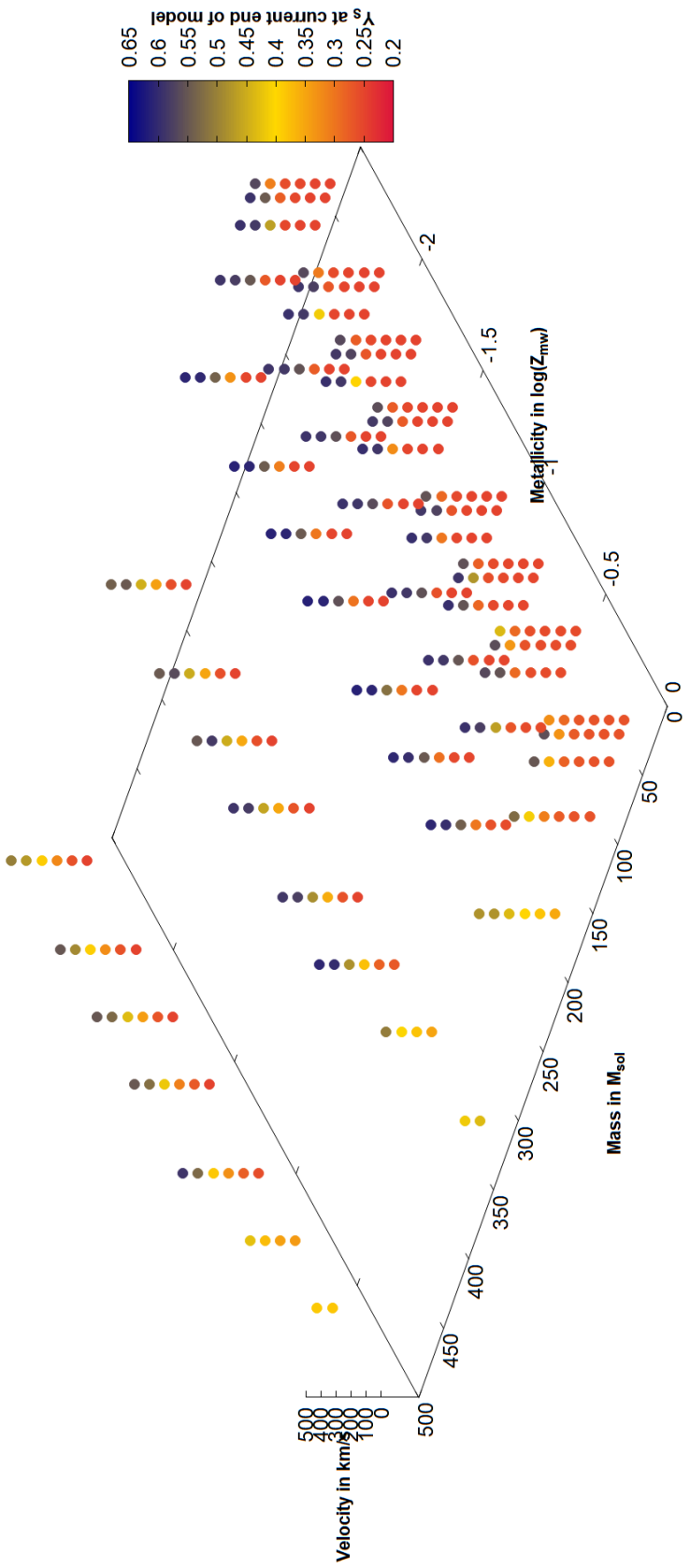

Figure 31: Plot of the Surface Helium Mass Fraction for the whole parameter space as a colour plot (cf. 3.1.4 and the caption of fig. 25). This figure (in contrast to fig. 25 and fig. 26) is showing the plot from the perspective of the mass-metallicity plane.

A.2 Appendix B

On the following pages the bulkplots from 4 are shown with minimal captions for better accessibility. Note also that the resolution of the images facilitates zoom-in as well.
For the more elaborate captions refer to the original figures.

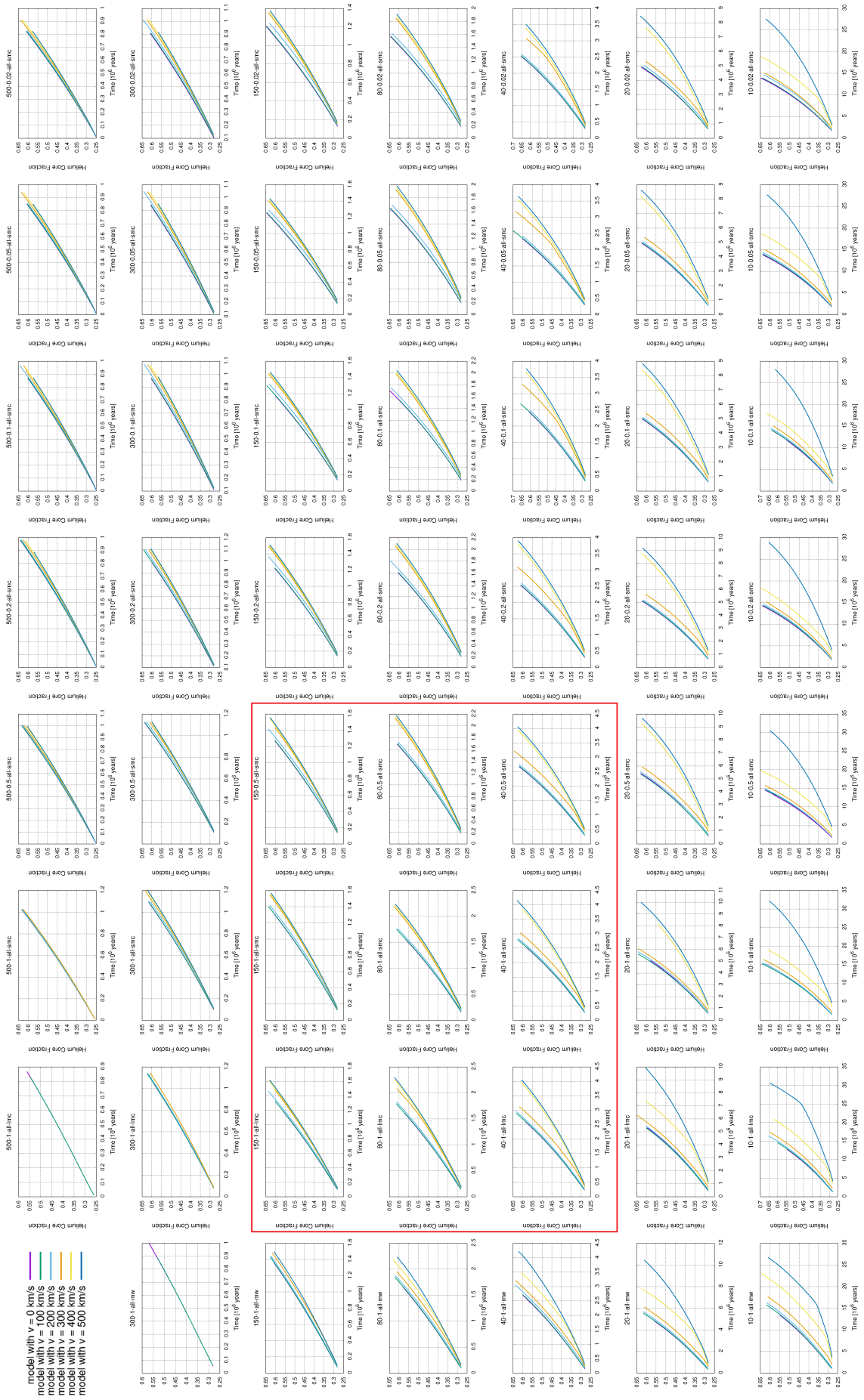

Figure 32: The bulkplot (cf. fig. 15) for the core helium mass fraction of the model sequences over time.

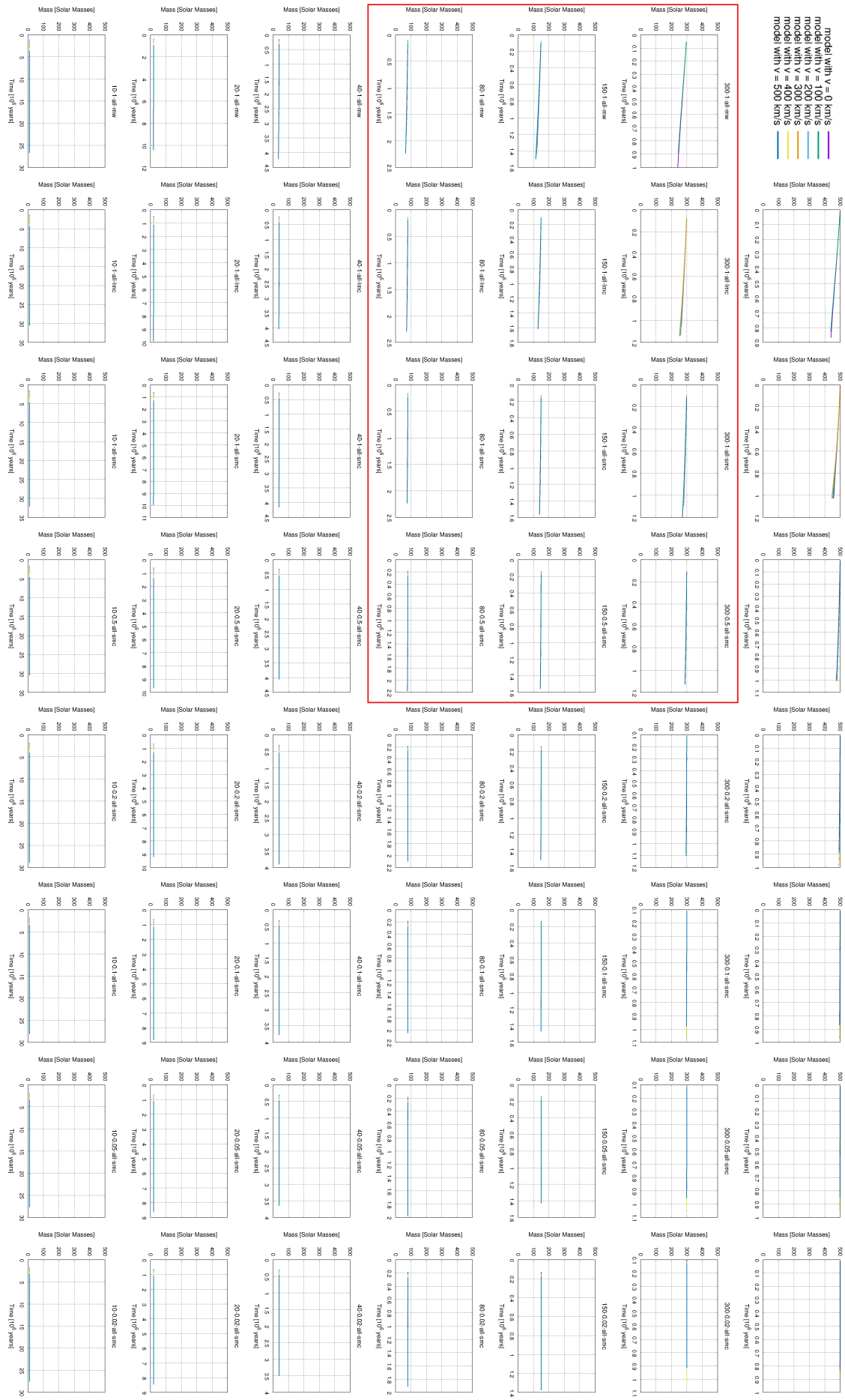

Figure 33: The bulkplot for the mass of the models (in $M_\odot$) over time (in $10^6\,yrs$) with a fixed mass scale and a flexible time scale.

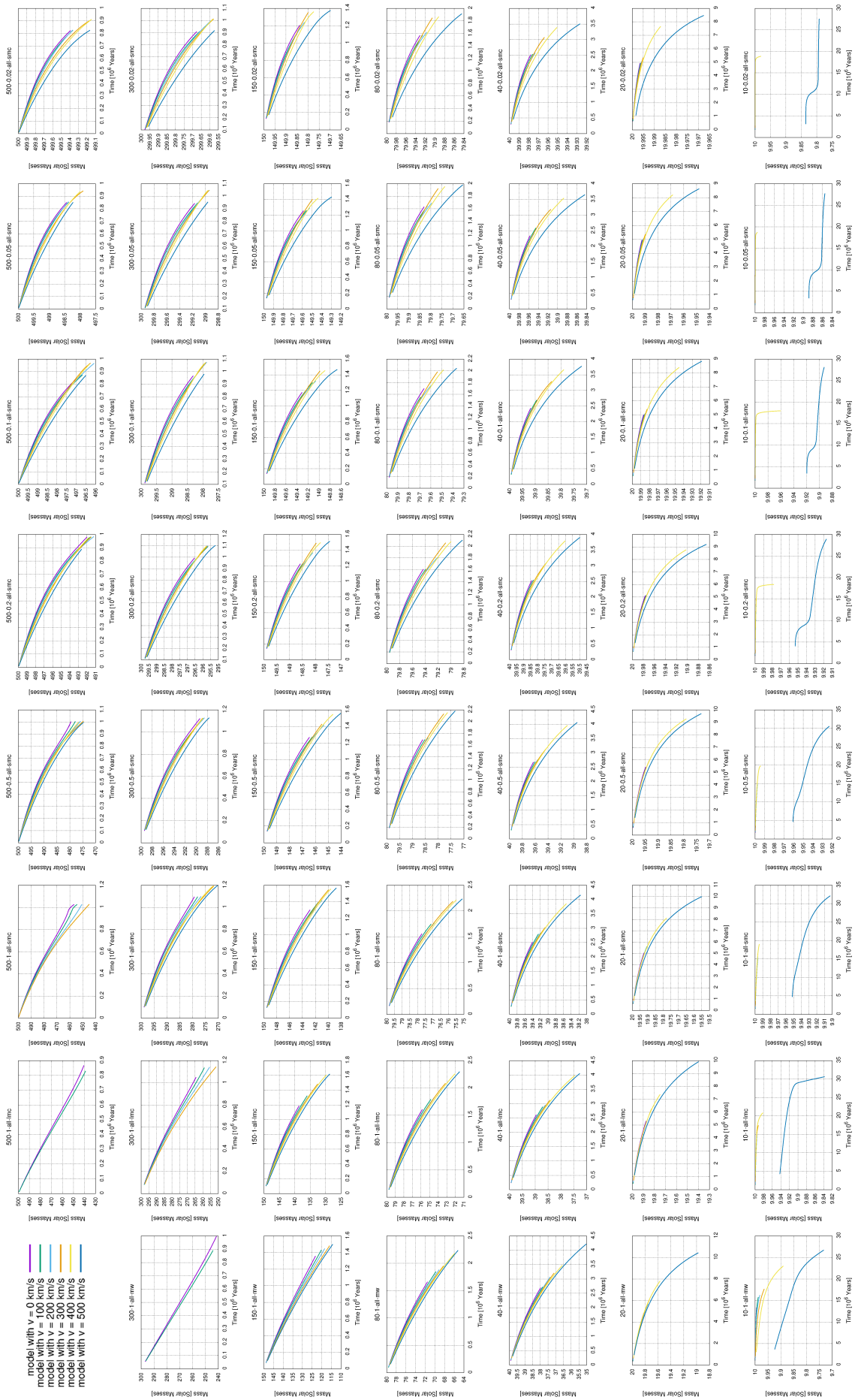

Figure 34: The bulkplot for the mass of the models (in $M_{\odot}$) over time (in $10^6 yrs$) with a flexible mass and time scale.

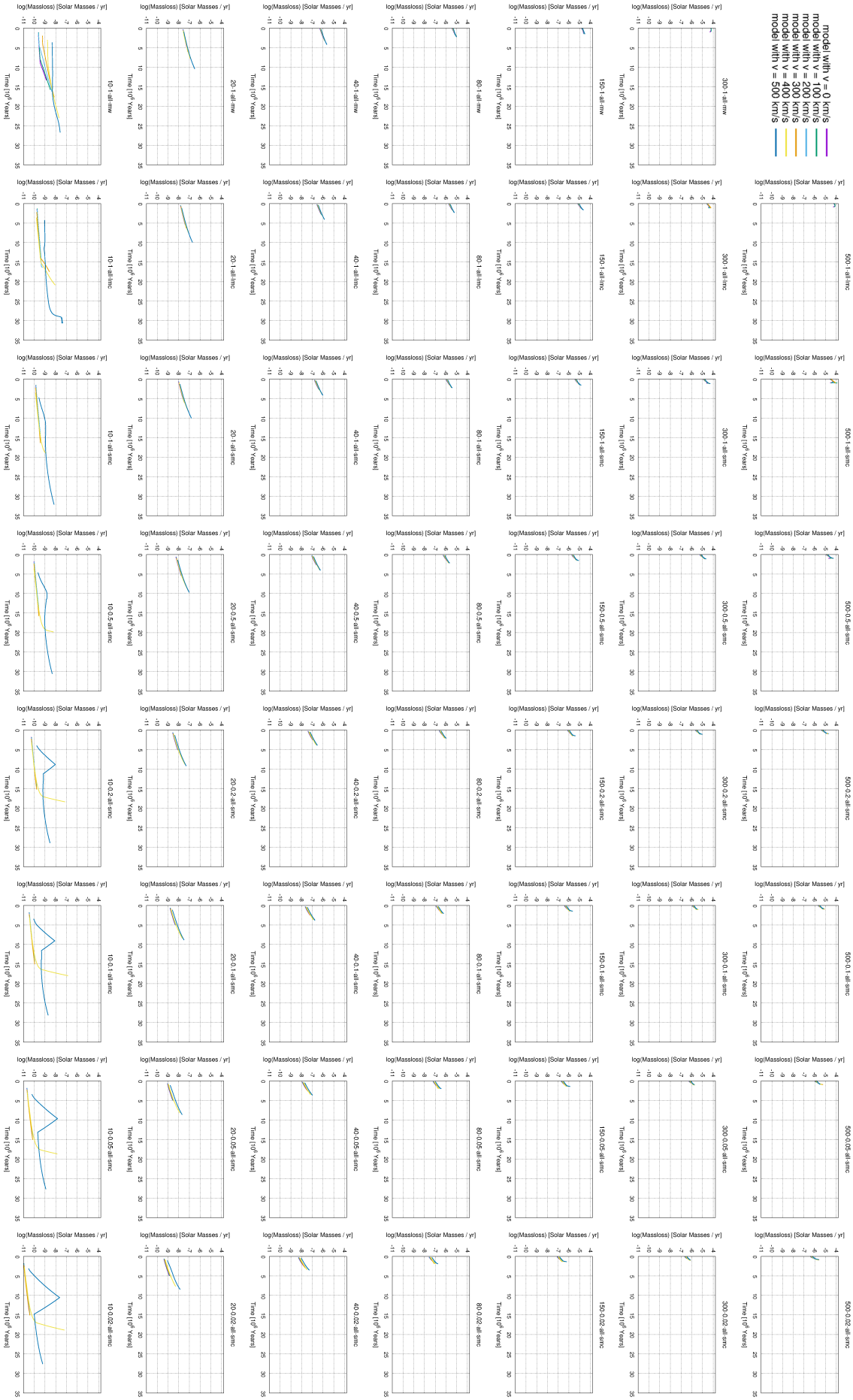

Figure 35: The bulkplot for the massloss of the models (in $M_\odot$) over time (in $10^6\,yrs$) with a fixed linear scale.

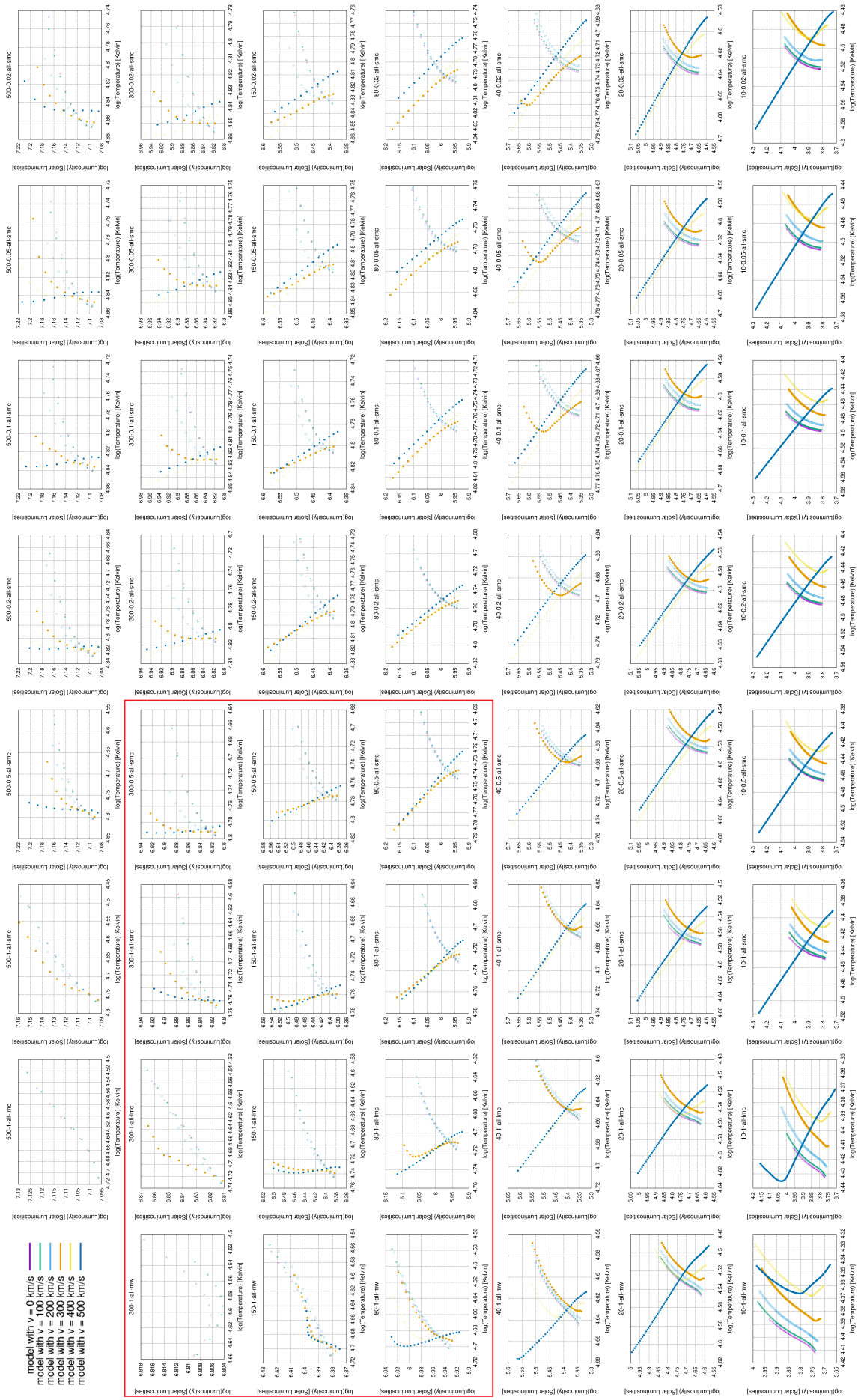

Figure 36: The bulkplot for the Hertzsprung-Russell diagram of the model sequences, displayed with isochrone dots in $10^5 yrs$ steps.

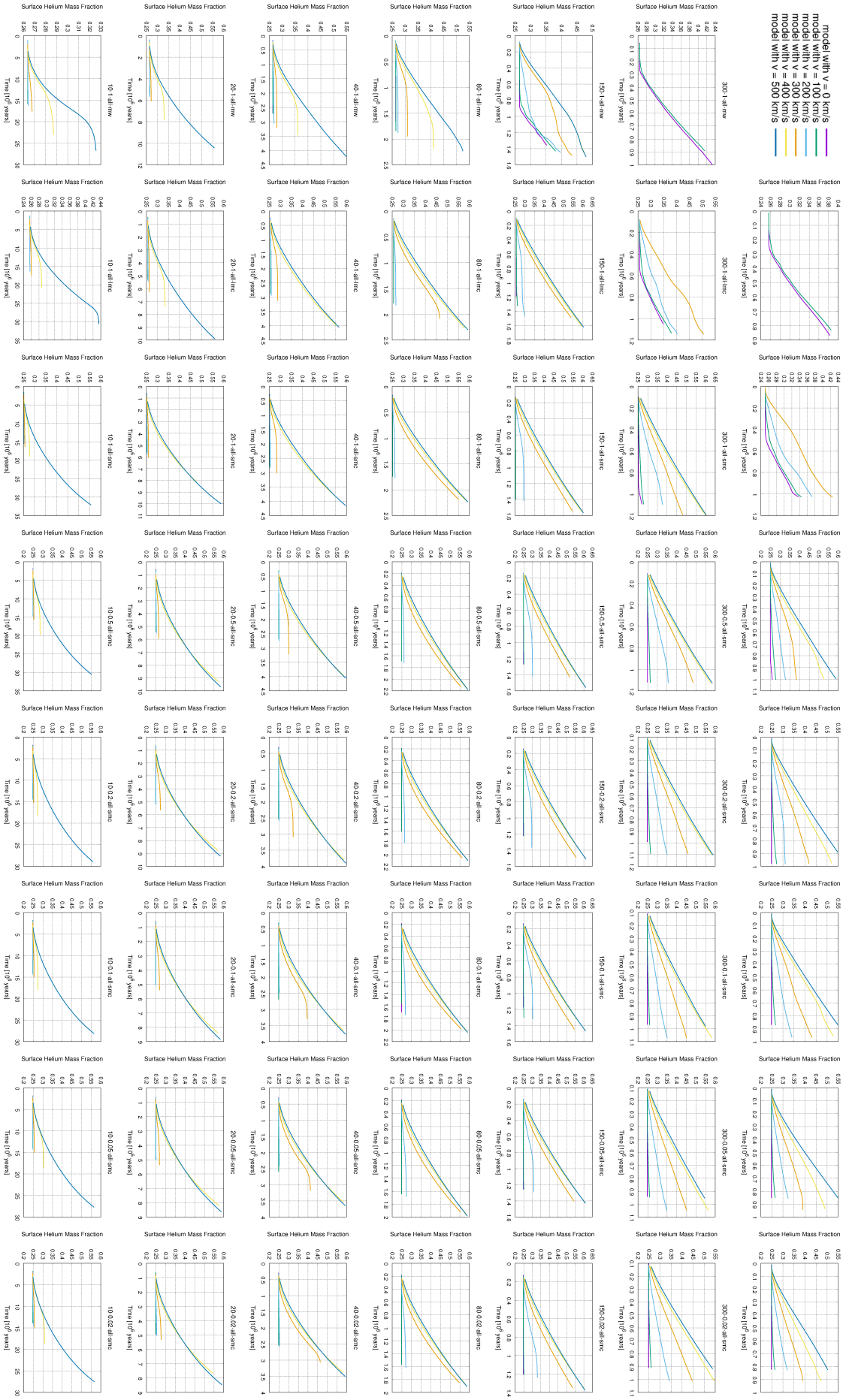

Figure 37: The bulkplot for the surface helium mass fraction of the models over time (in $10^6\,yrs$).

References

Aasi, J., Abbott, B. P., Abbott, R., Abbott, T., Abernathy, M. R., Ackley, K., ... Zweizig, J. (2015, mar). Advanced LIGO. *Classical and Quantum Gravity*, *32*(7), 074001. Retrieved from https://doi.org/10.1088/0264-9381/32/7/074001 doi: 10.1088/0264-9381/32/7/074001

Abbott, B. P., Abbott, R., Abbott, T. D., Abernathy, M. R., Acernese, F., Ackley, K., ... Zweizig, J. (2016, Feb). Observation of gravitational waves from a binary black hole merger. *Phys. Rev. Lett.*, *116*, 061102. Retrieved from https://link.aps.org/doi/10.1103/PhysRevLett.116.061102 doi: 10.1103/PhysRevLett.116.061102

Adelberger, E. G., García, A., Robertson, R. G. H., Snover, K. A., Balantekin, A. B., Heeger, K., ... et al. (2011, Apr). Solar fusion cross sections. ii. the pp chain and cno cycles. *Reviews of Modern Physics*, *83*(1), 195–245. Retrieved from http://dx.doi.org/10.1103/RevModPhys.83.195

Agrawal, P., Stevenson, S., Szécsi, D., & Hurley, J. (2021, December). A systematic study of super-Eddington envelopes in massive stars. *arXiv e-prints*, arXiv:2112.02801.

Agrawal, P., Szécsi, D., Stevenson, S., & Hurley, J. (2021, December). Explaining the differences in massive star models from various simulations. *arXiv e-prints*, arXiv:2112.02800.

Basumina, S., & Hurst, A. M. (2016). *Nuclear data sheets for a = 26* (Vol. 134). Retrieved from https://www.nndc.bnl.gov/ (visited on 2022-01-06, from nndc, ENSDF)

Bennett, N. J. (2018). A new source of lithium: Probing massive post main sequence low-metallicity stars in young globular clusters.

Boeltzig, A., Bruno, C., Cavanna, F., Cristallo, S., Davinson, T., Depalo, R., ... Wiescher, M. (2016, 04). Shell and explosive hydrogen burning. *The European Physical Journal A*, *52*. Retrieved from http://dx.doi.org/10.1140/epja/i2016-16075-4

Brott, I., de Mink, S. E., Cantiello, M., Langer, N., de Koter, A., Evans, C. J., ... Vink, J. S. (2011). Rotating massive main-sequence stars. *Astronomy*

and Astrophysics, *530*, A115. Retrieved from https://doi.org/10.1051/0004-6361/201016113

Brugaletta, V. (2021). The multi-phase interstellar medium in low-metallicity environments.

Cameron, A. G. W., & Fowler, W. A. (1971). Lithium and the s-process in red-giant stars. *Astrophys. J.*, *164*, 111–114. doi: 10.1086/150821

Cesar. (2021). *The hertzsprung russel diagram.* Retrieved from https://cesar.esa.int/index.php?Section=SSE_The_Hertzsprung_Russel_Diagram (visited on 2021-12-20)

Challouf, M., Nardetto, N., Domiciano de Souza, A., Mourard, D., Tallon-Bosc, I., Aroui, H., ... Mouelhi, M. (2017). Flattening and surface-brightness of the fast-rotating star sei with the visible vega/chara interferometer. *Astronomy and Astrophysics*, *604*, A51. Retrieved from https://doi.org/10.1051/0004-6361/201629934

Demtröder, W. (2014). *Experimentalphysik 4* (4th ed.). Springer Spektrum.

Eddington, A. S. (1988). *The internal constitution of the stars.* Cambridge University Press. doi: 10.1017/CBO9780511600005

Ekström, S., Georgy, C., Eggenberger, P., Meynet, G., Mowlavi, N., Wyttenbach, A., ... Maeder, A. (2012, January). Grids of stellar models with rotation. I. Models from 0.8 to 120 $M_{\odot}$ at solar metallicity (Z = 0.014). *Astronomy and Astrophysics*, *537*, A146. doi: 10.1051/0004-6361/201117751

Endal, A. S., & Sofia, S. (1976, November). The evolution of rotating stars. I. Method and exploratory calculations for a 7 M sun star. *The Astrophysical Journal*, *210*, 184-198. doi: 10.1086/154817

Fornalski, K. W. (2018). Simple empirical correction functions to cross sections of the photoelectric effect, compton scattering, pair and triplet production for carbon radiation shields for intermediate and high photon energies. *Journal of Physics Communications*, *2*(3), 035038. Retrieved from https://doi.org/10.1088/2399-6528/aab408

Gagnier, D., Rieutord, M., Charbonnel, C., Putigny, B., & Espinosa Lara, F. (2019). Critical angular velocity and anisotropic mass loss of rotating stars with radiation-driven winds. *Astronomy and Astrophysics*, *625*, A88. Retrieved from https://doi.org/10.1051/0004-6361/201834599 doi: 10.1051/0004-6361/201834599

Garcia, M., Evans, C., Bestenlehner, J., Bouret, J., Castro, N., Cerviño, M., ... Wofford, A. (2021). Massive stars in extremely metal-poor galaxies: A window into the past. *Experimental Astronomy*, *51* , 887-911. Retrieved from https://doi.org/10.1007/s10686-021-09785-x

Gatto, A., Walch, S., Naab, T., Girichidis, P., Wünsch, R., Glover, S. C. O., ... Puls, J. (2016, 12). The SILCC project – III. Regulation of star formation and outflows by stellar winds and supernovae. *Monthly Notices of the Royal Astronomical Society*, *466*(2), 1903-1924. Retrieved from https://doi.org/10.1093/mnras/stw3209 doi: 10.1093/mnras/stw3209

Grevesse, N., Noels, A., & Sauval, A. J. (1996, January). Standard Abundances. In S. S. Holt & G. Sonneborn (Eds.), *Cosmic abundances* (Vol. 99, p. 117).

Harwit, M. (2006). *Astrophysical Concepts* (4th ed.). Springer.

Heger, A., Langer, N., & Woosley, S. E. (2000, Jan). Presupernova evolution of rotating massive stars. i. numerical method and evolution of the internal stellar structure. *The Astrophysical Journal*, *528*(1), 368–396. Retrieved from http://dx.doi.org/10.1086/308158 doi: 10.1086/308158

Jin, J., Zhu, C., & Lü, G. (2015, 03). Convection and convective overshooting in stars more massive than 10 $M_{\odot}$. *Publications of the Astronomical Society of Japan*, *67*(2). Retrieved from https://doi.org/10.1093/pasj/psu153 (19) doi: 10.1093/pasj/psu153

Kippenhahn, R., Weigert, A., & Weiss, A. (2020). *Stellar Structure and Evolution* (2nd ed.). Springer.

Krtička, J., Owocki, S. P., & Meynet, G. (2011, Jan). Mass and angular momentum loss via decretion disks. *Astronomy and Astrophysics*, *527*, A84. Retrieved from http://dx.doi.org/10.1051/0004-6361/201015951

Kubátová, B., Szécsi, D., Sander, A. A. C., Kubát, J., Tramper, F., Krticka, J., ... Shenar, T. (2019). Low-metallicity massive single stars with rotation. *Astronomy and Astrophysics*, *623*, A8. Retrieved from https://doi.org/10.1051/0004-6361/201834360

Kuiper, G. P. (1938, November). The empirical mass-luminosity relation. *Astrophysical Journal*, *88*, 472. Retrieved from https://ui.adsabs.harvard.edu/abs/1938ApJ....88..472K

Lamers, H. J. G. L. M., & Fitzpatrick, E. L. (1988, January). The Relationship between the Eddington Limit, the Observed Upper Luminosity Limit for Massive Stars, and the Luminous Blue Variables. *Astrophysical Journal*, *324* , 279. doi: 10.1086/165894

Langer, N. (2012a). *Nucleosynthesis.* Retrieved from `https://astro.uni-bonn.de/~nlanger/siu_web/nucscript/Nucleo.pdf`

Langer, N. (2012b). Presupernova evolution of massive single and binary stars. *Annual Review of Astronomy and Astrophysics*, *50*(1), 107-164. Retrieved from `https://doi.org/10.1146/annurev-astro-081811-125534` doi: 10.1146/annurev-astro-081811-125534

Leloudas, G., Schulze, S., Krühler, T., Gorosabel, J., Christensen, L., Mehner, A., ... Wheeler, J. C. (2015, May). Spectroscopy of superluminous supernova host galaxies. A preference of hydrogen-poor events for extreme emission line galaxies. *MNRAS*, *449*(1), 917-932. doi: 10.1093/mnras/stv320

LoPresto, M. C. (2018). *The mass-lifetime relation.* Retrieved from `https://www.researchgate.net/publication/324624200_The_mass-lifetime_relation` (visited on 2021-12-23)

Marti, B. L., González, B., & Cesar. (2021). *Stellar evolution.* Cesar. Retrieved from `https://cesar.esa.int/upload/201801/stellarevolution_booklet_v2.pdf` (visited on 2021-12-20)

Mengel, J. G., Sweigart, A. V., Demarque, P., & Gross, P. G. (1979, August). Stellar evolution from the zero-age main sequence. *Astrophysical Journal Supplement Series*, *40*, 733-791. doi: 10.1086/190603

Peimbert, M., Luridiana, V., & Peimbert, A. (2007, September). Revised Primordial Helium Abundance Based on New Atomic Data. *The Astrophysical Journal*, *666*(2), 636-646. doi: 10.1086/520571

Piran, T. (2005, Jan). The physics of gamma-ray bursts. *Reviews of Modern Physics*, *76*(4), 1143–1210. Retrieved from `http://dx.doi.org/10.1103/RevModPhys.76.1143` doi: 10.1103/revmodphys.76.1143

Pols, O. R., Schröder, K.-P., Hurley, J. R., Tout, C. A., & Eggleton, P. P. (1998, August). Stellar evolution models for Z = 0.0001 to 0.03. *MNRAS*, *298*(2), 525-536. doi: 10.1046/j.1365-8711.1998.01658.x

Quimby, R. M., Yuan, F., Akerlof, C., & Wheeler, J. C. (2013, May). Rates of superluminous supernovae at z $\sim$ 0.2. *MNRAS*, *431*(1), 912-922. doi: 10.1093/mnras/stt213

Ratcliff, S. (2018). A new reservoir of lithium production in a metal-poor universe.

Ricci, F. (2019). Gravitational wave observations and future detectors. *Rendiconti Lincei. Scienze Fisiche e Naturali*, *30*, 57-64. Retrieved from `https://doi.org/10.1007/s12210-019-00840-6` doi: 10.1007/s12210-019-00840-6

Riley, J., Mandel, I., Marchant, P., Butler, E., Nathaniel, K., Neijssel, C., ... Vigna-Gómez, A. (2021, May). Chemically homogeneous evolution: a rapid population synthesis approach. *Monthly Notices of the Royal Astronomical Society*, *505*(1), 663–676. Retrieved from `http://dx.doi.org/10.1093/mnras/stab1291` doi: 10.1093/mnras/stab1291

Sackmann, I. J., & Boothroyd, A. I. (1998). *Creation of li-7 and destruction of he-3, be-9, b-10, and b-11 in low mass red giants, due to deep circulation.*

Sanyal, D., Grassitelli, L., Langer, N., & Bestenlehner, J. M. (2015, August). Massive main-sequence stars evolving at the Eddington limit. *Astronomy and Astrophysics*, *580*, A20. doi: 10.1051/0004-6361/201525945

Sanyal, D., Langer, N., Szécsi, D., Yoon, S.-C., & Grassitelli, L. (2017). Metallicity dependence of envelope inflation in massive stars. *Astronomy and Astrophysics*, *597*, A71. Retrieved from `https://doi.org/10.1051/0004-6361/201629612`

Soderberg, A. M., Kulkarni, S. R., Nakar, E., Berger, E., Cameron, P. B., Fox, D. B., ... McCarthy, P. J. (2006, August). Relativistic ejecta from x-ray flash xrf 060218 and the rate of cosmic explosions. *nature*, *442*, 1014-1017. Retrieved from `https://doi.org/10.1038/nature05087`

Suijs, M. (2006). Manual for the binary evolutionary code (bec) [Computer software manual]. Astronomical Institute Utrecht.

Szécsi, D., Langer, N., Yoon, S.-C., Sanyal, D., de Mink, S., Evans, C. J., & Dermine, T. (2015, Aug). Low-metallicity massive single stars with rotation. *Astronomy and Astrophysics*, *581*, A15. Retrieved from `http://dx.doi.org/10.1051/0004-6361/201526617`

Szécsi, D. (2017, July). How may short-duration GRBs form? A review of progenitor theories. *Contributions of the Astronomical Observatory Skalnate Pleso*, *47*(2), 108-115.

Szécsi, D., Agrawal, P., Wünsch, R., & Langer, N. (2022). Bonn optimized stellar tracks (boost) - simulated populations of massive and very massive stars for astrophysical applications. *Astronomy and Astrophysics*, *658*, A125. Retrieved from `https://doi.org/10.1051/0004-6361/202141536` doi: 10.1051/0004-6361/202141536

Szécsi, D., Mackey, J., & Langer, N. (2018). Supergiants and their shells in young globular clusters. *Astronomy and Astrophysics*, *612*, A55. Retrieved from `https://doi.org/10.1051/0004-6361/201731500`

Szécsi, D., & Wünsch, R. (2019). Role of supergiants in the formation of globular clusters. *The Astrophysical Journal*, *871*(1), 20. Retrieved from `https://doi.org/10.3847/1538-4357/aaf4be`

Ventura, P., Carini, R., & D'Antona, F. (2011, August). A deep insight into the Mg-Al-Si nucleosynthesis in massive asymptotic giant branch and super-asymptotic giant branch stars. *MNRAS*, *415*(4), 3865-3871. doi: 10.1111/j.1365-2966.2011.18997.x

Vink, J. S., de Koter, A., & Lamers, H. J. G. L. M. (2000, October). New theoretical mass-loss rates of O and B stars. *Astronomy and Astrophysics*, *362*, 295-309. Retrieved from `https://ui.adsabs.harvard.edu/abs/2000A&A...362..295V`

Vink, J. S., de Koter, A., & Lamers, H. J. G. L. M. (2001, Apr). Mass-loss predictions for o and b stars as a function of metallicity. *Astronomy and Astrophysics*, *369*(2), 574–588. Retrieved from `http://dx.doi.org/10.1051/0004-6361:20010127`

Vink, J. S., & Sander, A. A. C. (2021, Mar). Metallicity-dependent wind parameter predictions for ob stars. *Monthly Notices of the Royal Astronomical Society*, *504*(2), 2051–2061. Retrieved from `http://dx.doi.org/10.1093/mnras/stab902`

Vink, Jorick S. (2018). Very massive stars: a metallicity-dependent upper-mass limit, slow winds, and the self-enrichment of globular clusters. *Astronomy and Astrophysics*, *615*, A119. Retrieved from `https://doi.org/10.1051/0004-6361/201832773`

Walch, S., Girichidis, P., Naab, T., Gatto, A., Glover, S. C. O., Wünsch, R., ... Baczynski, C. (2015, November). The SILCC (SImulating the LifeCycle of molecular Clouds) project - I. Chemical evolution of the supernova-driven ISM. *MNRAS*, *454*(1), 238-268. doi: 10.1093/mnras/stv1975

Woosley, S. E. (1993, March). Gamma-Ray Bursts from Stellar Mass Accretion Disks around Black Holes. *Astrophysical Journal*, *405*, 273. doi: 10.1086/172359

Yoon, S. C., & Langer, N. (2005, November). Evolution of rapidly rotating metal-poor massive stars towards gamma-ray bursts. *Astronomy and Astrophysics*, *443*(2), 643-648. doi: 10.1051/0004-6361:20054030